Simple deformation measures for Discrete elastic rods and ribbons

Kevin Korner
Division of Engineering and Applied Science
California Institute of Technology
Pasadena, CA 91125, USA

Basile Audoly
Laboratoire de Mécanique des Solides
CNRS, Institut Polytechnique de Paris
91120 Palaiseau, France

Kaushik Bhattacharya
Division of Engineering and Applied Science
California Institute of Technology
Pasadena, CA 91125, USA

July 9, 2021

Abstract

The Discrete elastic rod method (Bergou *et al.*, 2008) is a numerical method for simulating slender elastic bodies. It works by representing the center-line as a polygonal chain, attaching two perpendicular directors to each segment, and defining discrete stretching, bending and twisting deformation measures and a discrete strain energy. Here, we investigate an alternative formulation of this model based on a simpler definition of the discrete deformation measures, which is equally consistent with the continuous rod model. The first and second gradients of the discrete deformation measures are derived in compact form, making it possible to evaluate the Hessian of the discrete strain energy exactly. A few numerical illustrations are given. The approach is also extended to the simulation of inextensible ribbons described by the Wunderlich model; both the developability constraint and the dependence of the energy of the strain gradients are handled naturally.

1 Introduction

The geometric non-linearity of thin elastic rods gives rise to a rich range of phenomena even when the strains are small, see e.g. [9, 30] for recent examples. So, the non-linear theory of rods has traditionally combined geometrically non-linearity with linear constitutive laws [1, 6]. However, recent interest has expanded beyond the linearly elastic regime, including viscous threads [14, 32], plastic and visco-plastic bars [17, 3, 4], visco-elastic rods [26], capillary elastic beams made of very soft materials [25]. Thin elastic ribbons may also be viewed in this class with a non-linear constitutive law that captures the complex deformation of the cross-sections [33, 40, 35, 37, 18, 5].

The study of instabilities, especially in the presence of complex constitutive relations. requires an accurate but efficient numerical method. Here, we build on the work of Bergou *et al.* [12] to propose a numerical method applicable to slender elastic structures in general. To keep the presentation focused, we limit our presentation to *elastic* rods: both linearly elastic and non-linear elastic constitutive laws are covered. Our contribution consists mainly in providing a discrete geometric description of slender rods. This kinematic building block is independent of the elastic constitutive law in our formulation, making the extension to non-elastic constitutive laws relatively straightforward, as discussed in section 4.

We follow the classical kinematic approach, and use the arc-length s in undeformed configuration as a Lagrangian coordinate. We denote the center-line of the rod in the current configuration as $\boldsymbol{x}(s)$ (boldface

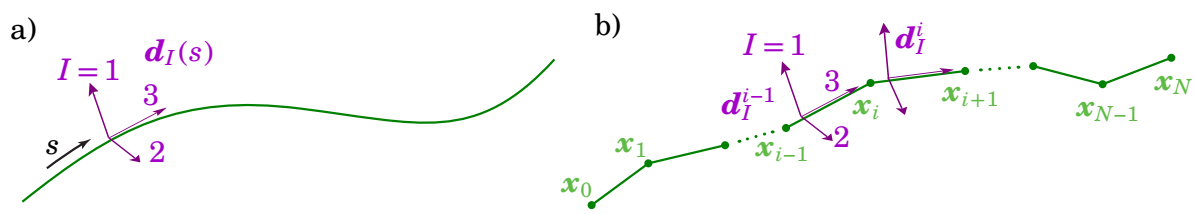

Figure 1.1: (a) A continuous elastic rod and (b) a discrete elastic rod. The adaptation condition from equations (1.1) and (2.6) is satisfied in both cases.

symbols denote vectors). We introduce an orthonormal set of vectors $(\boldsymbol{d}_I(s))_{1\leqslant I\leqslant 3}$, called the *directors*, to describe the orientation of the cross-section. We impose the *adaptation condition* that the director $\boldsymbol{d}_3$, matches the unit tangent $\boldsymbol{t}$ to the center-line:

$$\boldsymbol{d}_3(s) = \boldsymbol{t}(s), \text{ where } \boldsymbol{t}(s) = \frac{\boldsymbol{x}'(s)}{|\boldsymbol{x}'(s)|}. \tag{1.1}$$

Here $\boldsymbol{x}'(s) = \partial\boldsymbol{x}/\partial s$ denotes the derivative with respect to the arc-length s. Note that the adaptation condition does *not* impose any restriction on the actual deformation of the rod at microscopic scale; specifically, it does not require the deformed cross-section to be spanned by $\boldsymbol{d}_1$ and $\boldsymbol{d}_2$. Instead, it expresses the fact that the only role of the directors is to track the twisting motion of the cross-sections about the tangent. Equation (1.1) does not impose inextensibility either.

The rotation gradient $\boldsymbol{\kappa}(s)$, also known as the Darboux vector, is defined by

$$\boldsymbol{d}_I'(s) = \boldsymbol{\kappa}(s) \times \boldsymbol{d}_I(s), \qquad I = 1, 2, 3. \tag{1.2}$$

It exists and is unique since the directors are orthonormal. The deformation measures are

$$\kappa_{(I)}(s) = \boldsymbol{\kappa}(s) \cdot \boldsymbol{d}_I(s) \tag{1.3}$$

A fourth deformation measure is introduced to characterize how the center-line stretches, such as $\varepsilon(s) = \frac{1}{2}\left(\boldsymbol{x}'^2(s) - 1\right)$ (Green-Lagrange strain).

This kinematic description is common to all variants of the rod model. It is complemented by constitutive equations specifying either the stored energy density (in the case of a hyperelastic theory) or the reaction forces and moments as functions of the four deformation measures or their histories. The formulation is completed by imposing either equilibrium or balance of momenta. The resulting equations for linear elastic constitutive relations are known as the Kirchhoff equations for rods, and they can be derived variationally, see [38, 6]; we will not discuss them further.

Various strategies have been proposed to simulate the equations for thin rods numerically. In approaches based on the finite-element methods, it is challenging to represent the kinematic constraint of adaptation (1.1) between the unknown center-line $\boldsymbol{x}(s)$ and the unknown rotation representing the orthonormal directors $\boldsymbol{d}_I(s)$. Another approach is based on super-helices or super-clothoids: in these high-order approaches, the bending and twisting strain measures $\kappa_{(I)}(s)$ are discretized into constant or piecewise linear functions. The result is a highly accurate method which has been successfully applied to several challenging problems [13, 15, 16]. The price to pay, however, is that the reconstruction of the center-line in terms of the degrees of freedom is non-trivial and non-local. Additionally, some common boundary conditions, such as clamped-clamped conditions, must be treated using non-linear constraints.

A new approach called the Discrete elastic rods method was introduced by Bergou *et al.* [12]; see [24] for a recent primer. The Discrete elastic rod method is a low-order method, which starts out by discretizing the center-line into a polygonal chain with nodes $(\boldsymbol{x}_0, \ldots, \boldsymbol{x}_N)$. The tangents and material frames $\boldsymbol{d}_I^i$ are defined on the segments, see figure 1.1. The adaptation condition (1.1) is used to parameterize the material

frames $(\boldsymbol{d}_I^i)_{1\leqslant i\leqslant 3}$ in terms of the positions $(\boldsymbol{x}_{i-1}, \boldsymbol{x}_i)$ of the adjacent nodes and of a single twisting angle φ^i, as recalled in section 2.4. A discrete rotation gradient is obtained by comparing the orthonormal directors from adjacent segments: this yields a differential rotation living at an *interior vertex*, which must somehow be projected onto a material frame to yield the bending and twisting strain measures, see equation (1.3). The material frame, however, lives on *segments*. The original Discrete elastic rod formulation worked around this difficulty by introducing an additional director frame living on the nodes, obtained by averaging the director frames from the adjacent segments [12, 24]. In the present work, we solve this difficulty using a simpler approach which ultimately leads to a significantly more compact formulation, drawing inspiration from recent work on shearable rod models [21], and on the geometric analysis of discrete rods by [27]. Overall, the proposed formulation offers the following advantages:

- in line with the original Discrete rod model, it eliminates two out of the three degrees of freedom associated with the directors at each node using of the adaptation condition (1.1); this leads to a constraint-free formulation that uses degrees of freedom sparingly;
- the gradient and Hessian of the energy is derived in closed analytical form, see sections 3 and 4;
- the simpler definition of the discrete strain leads to a compact formulation: all the formulas required for the evaluation of the gradient and Hessian of the discrete elastic energy are included in sections 2.7 and 3;
- the proposed deformation measures have a clear geometric interpretation: in the context of inextensible ribbons, for example, a discrete developability condition can easily be formulated in terms of the new set of discrete strains, see section 4.2.
- the kinematic description can easily be combined with various constitutive models to produce discrete models for elastic rods, inextensible ribbons, viscous or visco-elastic rods, etc., as discussed in section 4.

2 Discrete bending and twisting deformation measures

2.1 A compendium on quaternions

Rod models make use of rotations in the three-dimensional space. These rotations are conveniently represented using quaternions. Here, we provide a brief summary of quaternions and their main properties.

A quaternion $q \in \mathbb{Q}$ can be seen as a pair made up of a scalar $s \in \mathbb{R}$ and a vector $\boldsymbol{v} \in \mathbb{R}^3$, $q = (s, \boldsymbol{v})$. Identifying the scalar s and the vector $\boldsymbol{v}$ with the quaternions $(s, \boldsymbol{0})$ and $(0, \boldsymbol{v})$, respectively, one has the quaternion decomposition

$$q = s + \boldsymbol{v}.$$

The product of two quaternions $q_1 = (s_1, \boldsymbol{v}_1)$ and $q_2 = (s_2, \boldsymbol{v}_2)$ is defined as

$$q_1\, q_2 = (s_1\, s_2 - \boldsymbol{v}_1 \cdot \boldsymbol{v}_2) + (s_1 \boldsymbol{v}_2 + s_2 \boldsymbol{v}_1 + \boldsymbol{v}_1 \times \boldsymbol{v}_2). \tag{2.1}$$

The product is non-commutative.

A unit quaternion $r = s + \boldsymbol{v}$ is a quaternion such that $s^2 + |\boldsymbol{v}|^2 = 1$. Unit quaternions represent rotations in the three-dimensional Euclidean space, in the following sense. Define $\bar{r} = s - \boldsymbol{v}$ as the quaternion conjugate to r. Define the action of the unit quaternion r on an arbitrary vector $\boldsymbol{w}$ as

$$r * \boldsymbol{w} = r\, \boldsymbol{w}\, \bar{r},$$

where the left-hand side defines a linear map on the set of vectors $\boldsymbol{w}$, and the right-hand side is a double product of quaternions. It can be shown that *(i)* the quaternion $r * \boldsymbol{w}$ is a pure vector, *(ii)* the mapping $\boldsymbol{w} \to r * \boldsymbol{w}$ is a rotation in Euclidean space, *(iii)* the quaternion r can be written as $r = \pm r_{\boldsymbol{n}}(\theta)$ where

$$r_{\boldsymbol{n}}(\theta) = \cos\frac{\theta}{2} + \boldsymbol{n}\, \sin\frac{\theta}{2} = \exp\frac{\boldsymbol{n}\,\theta}{2}, \tag{2.2}$$

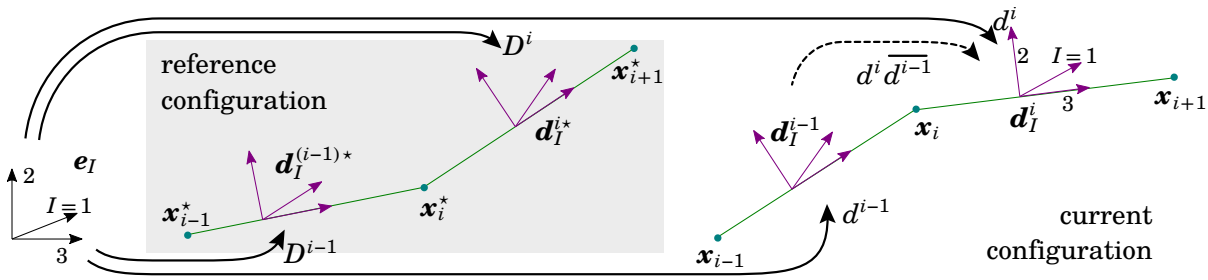

Figure 2.1: A node $\boldsymbol{x}_i$, its adjacent segments, and the adjacent nodes $\boldsymbol{x}_{i\pm1}$ in reference (gray background) and current (white background) configurations. Director frames, shown in purple, are represented by a unit quaternion, whose action on the Cartesian frame $\boldsymbol{e}_I$ yields the director frame.

θ is the angle of the rotation, and $\boldsymbol{n}$ is a unit vector subtending the axis of the rotation. Note that both unit quaternions $+r_{\boldsymbol{n}}(\theta)$ and $-r_{\boldsymbol{n}}(\theta)$ represent the same rotation.

Given two unit quaternions r_1 and r_2, consider the product $r_2\, r_1$: for any vector $\boldsymbol{w}$, the equality $(r_2\, r_1) * \boldsymbol{w} = r_2\, r_1\, \boldsymbol{w}\, \overline{r_2\, r_1} = r_2\, r_1\, \boldsymbol{w}\, \overline{r_1}\, \overline{r_2} = r_2 * (r_1 * \boldsymbol{w})$ shows that the unit quaternion $r_2\, r_1$ represents the *composition* of the rotations associated with r_1, applied first, and with r_2, applied last. The multiplication of unit quaternions is therefore equivalent to the composition of rotations. In view of this, we will *identify* rotations with unit quaternions. The inverse of the rotation r will accordingly be identified with the conjugate $\overline{r}$.

2.2 Parallel transport

Parallel transport plays a key role in the Discrete elastic rods model, by allowing one to define twistless configurations of the material frames in an intrinsic way. For two unit vectors $\boldsymbol{a}$ and $\boldsymbol{b}$ such that $\boldsymbol{b} \neq -\boldsymbol{a}$, the parallel transport from $\boldsymbol{a}$ to $\boldsymbol{b}$ is the rotation mapping $\boldsymbol{a}$ to $\boldsymbol{b}$, whose axis is along the binormal $\boldsymbol{a} \times \boldsymbol{b}$: parallel transport can be interpreted geometrically as the rotation mapping $\boldsymbol{a}$ to $\boldsymbol{b}$ and tracing out the shortest path on the unit sphere [12].

An explicit expression of the parallel transport from $\boldsymbol{a}$ to $\boldsymbol{b}$ in terms of unit quaternions is [27]

$$p_{\boldsymbol{a}}^{\boldsymbol{b}} = \sqrt{\frac{1 + \boldsymbol{a} \cdot \boldsymbol{b}}{2}} + \frac{1}{2}\, \frac{\boldsymbol{a} \times \boldsymbol{b}}{\sqrt{\frac{1+\boldsymbol{a}\cdot\boldsymbol{b}}{2}}}. \tag{2.3}$$

The proof is as follows. First it can be verified that $p_{\boldsymbol{a}}^{\boldsymbol{b}}$ is a unit quaternion, as can be shown by using the identity $\frac{|\boldsymbol{a}\times\boldsymbol{b}|^2}{1+\boldsymbol{a}\cdot\boldsymbol{b}} = \frac{1-(\boldsymbol{a}\cdot\boldsymbol{b})^2}{1+\boldsymbol{a}\cdot\boldsymbol{b}} = 1 - \boldsymbol{a}\cdot\boldsymbol{b}$. Second, the rotation $p_{\boldsymbol{a}}^{\boldsymbol{b}}$ indeed maps $\boldsymbol{a}$ to

$$p_{\boldsymbol{a}}^{\boldsymbol{b}} * \boldsymbol{a} = p_{\boldsymbol{a}}^{\boldsymbol{b}}\, \boldsymbol{a}\, \overline{p_{\boldsymbol{a}}^{\boldsymbol{b}}} = \boldsymbol{b}, \tag{2.4}$$

as can be checked. Finally, the axis of $p_{\boldsymbol{a}}^{\boldsymbol{b}}$ is indeed about the binormal $\boldsymbol{a} \times \boldsymbol{b}$: equation (2.2) shows that the vector part of the unit quaternion is aligned with the rotation axis and equation (2.3) shows that the vector part of $p_{\boldsymbol{a}}^{\boldsymbol{b}}$ is aligned with $\boldsymbol{a} \times \boldsymbol{b}$.

For two units vectors $\boldsymbol{a}$ and $\boldsymbol{b}$ such that $\boldsymbol{a} = -\boldsymbol{b}$, the parallel transport $p_{\boldsymbol{a}}^{\boldsymbol{b}}$ is ill-defined.

2.3 Reference and current configurations

A configuration of the discrete rod is defined by a set of nodes $\boldsymbol{x}_i$ indexed by an integer i, $0 \leqslant i \leqslant N$. We consider an open rod having unconstrained endpoints $\boldsymbol{x}_0$ and $\boldsymbol{x}_N$ for the moment; alternate boundary conditions such as periodic or clamped boundary conditions are discussed later. For simplicity, we limit attention to the case where the nodes are equally spaced in the undeformed configuration, *i.e.*, the undeformed length ℓ^j is independent of the segment index j: it is denoted as

$$\ell^j = \ell.$$

In addition to the undeformed configuration, the simulation deals with two configurations shown in figure 2.1:

- **Reference configuration** (shown with a gray background in the figure). The only role of the reference configuration is to allow a parameterization of the current configuration. It does not bear any physical meaning and its choice does not affect the results of the simulations. It is chosen for convenience.

  In the reference configuration, the position of node i is denoted by $\boldsymbol{x}_i^\star$. The orthonormal frame of directors on segment i connecting nodes $\boldsymbol{x}_i^\star$ and $\boldsymbol{x}_{i+1}^\star$ is denoted as $(\boldsymbol{d}_I^{i\star})_{I\in\{1,2,3\}}$. The adaptation condition from equation (1.1) requires that the third director $\boldsymbol{d}_3^{j\star}$ coincides with the unit tangent $\boldsymbol{T}^j$ to the segment in reference configuration,

$$\boldsymbol{d}_3^{j\star} = \boldsymbol{T}^j, \text{ where } \boldsymbol{T}^j = \frac{\boldsymbol{x}_{j+1}^\star - \boldsymbol{x}_j^\star}{|\boldsymbol{x}_{j+1}^\star - \boldsymbol{x}_j^\star|}. \tag{2.5}$$

- **Current configuration** (shown with a white background). The current configuration is the physical configuration of the rod and is the unknown in a simulation. It is parameterized by the degrees of freedoms (see section 2.7).

  In the current configuration, the center-line of the rod is defined by the node positions $\boldsymbol{x}_i$. On segment i connecting the nodes $\boldsymbol{x}_i$ and $\boldsymbol{x}_{i+1}$, the directors are denoted as $(\boldsymbol{d}_I^i)_{I\in\{1,2,3\}}$. The adaptation condition from equation (1.1) requires

$$\boldsymbol{d}_3^j = \boldsymbol{t}^j, \text{ where } \boldsymbol{t}^j = \frac{\boldsymbol{x}_{j+1} - \boldsymbol{x}_j}{|\boldsymbol{x}_{j+1} - \boldsymbol{x}_j|}. \tag{2.6}$$

As shown in the figure, the orthonormal director frames $(\boldsymbol{d}_I^{j\star})_{1\leqslant I\leqslant 3}$ and $(\boldsymbol{d}_I^j)_{1\leqslant I\leqslant 3}$ are represented by unit quaternions D^j and d^j, respectively, that yield the directors when applied on the Cartesian basis $\boldsymbol{e}_I$:

$$D^j * \boldsymbol{e}_I = \boldsymbol{d}_I^{j\star} \qquad d^j * \boldsymbol{e}_I = \boldsymbol{d}_I^j \qquad \text{for } I = 1,2,3 \tag{2.7}$$

The quaternions $d^{j\star}$ and d^j therefore represent the rotations $\sum_{I=1}^3 \boldsymbol{d}_I^{j\star} \otimes \boldsymbol{e}_I$ and $\sum_{I=1}^3 \boldsymbol{d}_I^j \otimes \boldsymbol{e}_I$, respectively. They fully describe their respective frames.

The reference and current configurations are not assumed to be close to one another. However, our parameterization introduces a weak restriction: the reference configuration must be chosen such that the angle of the rotation $\left(d^j\,\overline{D}^j\right)$ mapping $\boldsymbol{d}_I^{j\star}$ to $\boldsymbol{d}_I^j$ does not come close to π, in any of the segments j. This condition is fulfilled by resetting periodically the reference configuration to the current configuration:

- in dynamic simulations, this reset is typically done at the end of any time step;
- in equilibrium problems, it is typically done whenever an equilibrium has been found and the load is incremented.

In principle, it is even possible to reset the reference configuration in the middle of the Newton-Raphson loop solving the time step (in the dynamic case) or the non-linear equilibrium (in the static case), but special care is required as this amounts to changing the parameterization of the unknown in the middle of the iterations.

All the applications shown at the end of this paper deal with the static case, *i.e.*, they involve the calculation of equilibria for a series of load values: our simulations are initialized with the reference configuration $\boldsymbol{x}_i^\star$, $\boldsymbol{d}_I^{j\star}$ representing a simple starting point which is typically a straight or circular equilibrium configuration without any load (see the example description for further details). The reference configuration is reset each time an equilibrium has been found.

2.4 Centerline-twist representation

In this section, we introduce a parameterization that provides a concise representation of the current configuration that is at the heart of the Discrete elastic rod method. All quantities from the reference configuration,

such as the node positions $\boldsymbol{x}_i^\star$, unit tangents $\boldsymbol{T}^j$, material frames $\boldsymbol{d}_3^{j\star}$ and associated rotations D^j, are known. We proceed to analyze the current configuration. A key observation is that equation (2.6) yields the tangent director $\boldsymbol{d}_3^j$ as a function of the node positions $\boldsymbol{x}_i$: if the nodes are prescribed, the full frame of directors $\boldsymbol{d}_I^j$ can only twist about this tangent. The three directors $(\boldsymbol{d}_I^j)_{1\leqslant I\leqslant 3}$ on segment j, as well as the associated unit quaternion d^j by equation (2.7), can therefore be parameterized in terms of

- the adjacent nodes positions $\boldsymbol{x}_j$ and $\boldsymbol{x}_{j+1}$,
- a scalar twist angle φ^j.

The parameterization used by the Discrete elastic rod method writes [12, 11, 2]

$$d^j(\boldsymbol{x}_j, \varphi^j, \boldsymbol{x}_{j+1}) = p^j(\boldsymbol{x}_j, \boldsymbol{x}_{j+1})\, r_{\boldsymbol{T}^j}(\varphi^j)\, D^j, \tag{2.8}$$

where $\boldsymbol{x}_j$ and $\boldsymbol{x}_{j+1}$ are the positions of the adjacent nodes, φ^j is the twisting angle,

$$p^j(\boldsymbol{x}_j, \boldsymbol{x}_{j+1}) = p_{\boldsymbol{T}^i}^{\boldsymbol{t}^i(\boldsymbol{x}_j, \boldsymbol{x}_{j+1})} \tag{2.9}$$

is the parallel transport from the reference unit tangent $\boldsymbol{T}^i$ to the current unit tangent $\boldsymbol{t}^i(\boldsymbol{x}_j, \boldsymbol{x}_{j+1})$ given as a function of the node positions by equation (2.6), $r_{\boldsymbol{T}^j}(\varphi^j) = \cos\frac{\varphi^j}{2} + \boldsymbol{T}^j \sin\frac{\varphi^j}{2}$ is the rotation about $\boldsymbol{T}^j$ with angle φ^j, see equation (2.2), and D^j is the unit quaternion associated with the reference configuration of the directors, see equation (2.7).

Using equations (2.7), (2.5) and (2.4), we have $\boldsymbol{d}_3^j = d^j(\boldsymbol{x}_j, \varphi^j, \boldsymbol{x}_{j+1}) * \boldsymbol{e}_3 = p^j(\boldsymbol{x}_j, \boldsymbol{x}_{j+1}) * (r_{\boldsymbol{T}}(\varphi^j, \boldsymbol{T}^j) * (D^j * \boldsymbol{e}_3)) = p_{\boldsymbol{T}^i}^{\boldsymbol{t}^i} * (r_{\boldsymbol{T}^j}(\varphi^j) * \boldsymbol{T}^j) = p_{\boldsymbol{T}^i}^{\boldsymbol{t}^i} * \boldsymbol{T}^j = \boldsymbol{t}^j$: the parameterization (2.8) of the directors satisfies the adaptation constraint in (2.6) automatically.

This yields a parameterization of the rod in terms of the degrees of freedom vector

$$\boldsymbol{X} = (\boldsymbol{x}_0, \varphi^0, \boldsymbol{x}_1, \varphi^1, \boldsymbol{x}^2, \cdots, \boldsymbol{x}_{n-1}, \varphi^{n-1}, \boldsymbol{x}_n), \tag{2.10}$$

where the nodes positions $\boldsymbol{x}_i$ are read off directly from $\boldsymbol{X}$ and the directors are reconstructed using equations (2.7) and (2.8). It is called the *centerline-twist representation*.

As observed in section 2.2, the parallel transport in equation (2.9) is singular if $\boldsymbol{t}^i(\boldsymbol{x}_j, \boldsymbol{x}_{j+1}) = -\boldsymbol{T}^i$, *i.e.*, if any one of the tangents flips by an angle π between the reference and current configuration. The periodic reset of the reference configuration described earlier in section 2.3 prevents this from happening.

Note that in the original paper of [12], parallel transport was used to move the directors from one segment to an adjacent segment (*spatial* parallel transport). This makes the directors dependent on the degrees of freedom associated with all the nodes and segments located on one side of the directors. Here, like in subsequent work by the same authors [11, 2], we use parallel transport 'in time': in equation (2.8), $p^j(\boldsymbol{x}_j, \boldsymbol{x}_{j+1})$ serves to parameterize the directors in current configuration in terms of the same set of directors in reference configuration. With this approach, the directors are a function of the *local* degrees of freedom, as implied by the notation $d^j(\boldsymbol{x}_j, \varphi^j, \boldsymbol{x}_{j+1})$ in equation (2.8).

2.5 Lagrangian rotation gradient

The rotation mapping one director frame $(\boldsymbol{d}_I^{i-1})_{I=1,2,3}$ to the adjacent director frame $(\boldsymbol{d}_I^i)_{I=1,2,3}$ is shown by the dashed arrow on top of figure 2.1. It captures the variation of the frame along the rod, and it is the discrete counterpart of the rotation gradient $\boldsymbol{\kappa}(s)$ introduced in equation (1.2). Using equation (2.7), it can be written as the composition of the rotations $\overline{d^{i-1}}$ and d^i:

$$d^i\,\overline{d^{i-1}} : \boldsymbol{d}_I^{i-1} \mapsto \boldsymbol{d}_I^i.$$

This rotation is an Eulerian quantity: like its continuous counterpart $\boldsymbol{\kappa}(S)$, it is not invariant when the rod rotates rigidly. We seek to define a Lagrangian version q_i that is invariant by rigid-body rotations. We define the Lagrangian rotation gradient to be

$$q_i(\boldsymbol{x}_{i-1}, \varphi^{i-1}, \boldsymbol{x}_i, \varphi^i, \boldsymbol{x}_{i+1}) := \overline{d^{i-1}}(\boldsymbol{x}_{i-1}, \varphi^{i-1}, \boldsymbol{x}_i)\, d^i(\boldsymbol{x}_i, \varphi^i, \boldsymbol{x}_{i+1}). \tag{2.11}$$

A similar definition has been used by [21] in the context of shearable rods, for which the constraint in equation (1.1) is not enforced, and in the geometric analysis of [27]. However, our definition is different from that of [12] who use $q_i^{\text{avg}} = \overline{d}_i^{\dagger}\,(d^i\,\overline{d^{i-1}})\,d_i^{\dagger}$ where $d_i^{\dagger}$ is some average of the adjacent frames d^{i-1} and d^i.

We now explain why this definition represents a Lagrangian rotation gradient. One way to define a Lagrangian rotation gradient, is to pull back the Eulerian rotation gradient $d^i\,\overline{d^{i-1}}$ to the reference configuration. However, the discreteness of our representation raises a difficulty: the frames are defined on the segment while the Eulerian rotation gradient $d^i\,\overline{d^{i-1}}$ is defined on the nodes. So, we could use the frame associated with the segment on the left of the node for the pull back by defining $q_i^{\text{left}} = \overline{d^{i-1}}\,(d^i\,\overline{d^{i-1}})\,d^{i-1}$, but this biases the choice on the left. Or, we could use the right counter-part, $q_i^{\text{right}} = \overline{d^i}\,(d^i\,\overline{d^{i-1}})\,d^i$, but this biases the choice to the right. However, this difficulty is apparent only: elementary calculations shows that these are in fact identical

$$q_i^{\text{left}} = \overline{d^{i-1}}\,d^i\,\left(\overline{d^{i-1}}\,d^{i-1}\right) = \overline{d^{i-1}}\,d^i = q_i, \quad q_i^{\text{right}} = \left(\overline{d^i}\,d^i\right)\,\overline{d^{i-1}}\,d^i = \overline{d^{i-1}}\,d^i = q_i, \tag{2.12}$$

thereby justifying our definition.

The unit quaternion q_i introduced in equation (2.11) is the discrete analogue of the pull-back $(\boldsymbol{e}_I \otimes \boldsymbol{d}_I(s)) \cdot \boldsymbol{\kappa}(s)$ of the rotation gradient $\boldsymbol{\kappa}(s)$ used in the continuous rod theory, whose components $\kappa_J(s) = \boldsymbol{e}_J \cdot [(\boldsymbol{e}_I \otimes \boldsymbol{d}_I(s)) \cdot \boldsymbol{\kappa}(s)] = \boldsymbol{d}_J(s) \cdot \boldsymbol{\kappa}(s)$ define the bending and twisting measures. In the following section, bending and twisting are similarly extracted from the unit quaternion q_i.

2.6 Bending and twisting deformation measures

The discrete bending and twisting deformation measures are defined as the components of the pure vector,

$$\boldsymbol{\kappa}_i(\boldsymbol{x}_{i-1}, \varphi^{i-1}, \boldsymbol{x}_i, \varphi^i, \boldsymbol{x}_{i+1}) = q_i - \overline{q}_i. \tag{2.13}$$

This $\boldsymbol{\kappa}_i$ is twice the vector part $\mathcal{I}(q_i) = \frac{q_i - \overline{q}_i}{2}$ of the quaternion q_i, which shows that it is indeed a vector. Let $\kappa_{i,I}$ denote its components in the Cartesian basis, such that $\boldsymbol{\kappa}_i = \sum_{I=1}^{3} \kappa_{i,I}\,\boldsymbol{e}_I$. The first two components $\kappa_{i,1}$ and $\kappa_{i,2}$ can be interpreted as measures of bending about the transverse directors $\boldsymbol{d}_1^j$ and $\boldsymbol{d}_2^j$, while the third component $\kappa_{i,3}$ is a discrete measure of twisting. Like q_i, these are *integrated* versions of their smooth counterparts, that are proportional to the discretization length ℓ; this will be taken into account when setting up a discrete strain energy.

2.7 Summary

The current configuration is reconstructed in terms of the degrees of freedom $\boldsymbol{X}$ from equation (2.10) as follows:

- the node positions $\boldsymbol{x}_i$ are directly extracted from $\boldsymbol{X}$, see equation (2.10),
- the unit tangents $\boldsymbol{t}^j(\boldsymbol{x}_j, \boldsymbol{x}_{j+1})$ are obtained from equation (2.6),
- parallel transport $p^j(\boldsymbol{x}_j, \boldsymbol{x}_{j+1})$ is obtained by combining equations (2.9) and (2.3),
- the director frames $d^j(\boldsymbol{x}_j, \varphi^j, \boldsymbol{x}_{j+1})$ are obtained from equation (2.8),
- the rotation gradient $q_i(\boldsymbol{x}_{i-1}, \varphi^{i-1}, \boldsymbol{x}_i, \varphi^i, \boldsymbol{x}_{i+1})$ is available from equation (2.11),
- the bending and twisting deformation vector $\boldsymbol{\kappa}_i(\boldsymbol{x}_{i-1}, \varphi^{i-1}, \boldsymbol{x}_i, \varphi^i, \boldsymbol{x}_{i+1})$ is calculated from equation (2.13).

Finally, a possible definition of the discrete stretching measure on segment j joining nodes $\boldsymbol{x}_j$ and $\boldsymbol{x}_{j+1}$ is

$$\varepsilon^j(\boldsymbol{x}_j, \boldsymbol{x}_{j+1}) = \frac{1}{2}\left(\frac{(\boldsymbol{x}_{j+1} - \boldsymbol{x}_j)^2}{\ell} - \ell\right), \tag{2.14}$$

see for instance [26]. Here, ℓ denotes the undeformed length of the segments, which is different from the length $|\boldsymbol{x}^\star_{j+1} - \boldsymbol{x}^\star_j|$ in reference configuration. This discrete stretching measure is an integrated version of the continuous strain $\varepsilon(S)$, like the discrete bending and twisting deformation measures $\kappa_{i,I}$. The particular definition of the stretching measure ε^j in equation (2.14) requires the evaluation of the *squared* norm and not of the norm itself, which simplifies the calculation of the gradient significantly.

2.8 Interpretation of the discrete deformation measures

We now show that the discrete deformation measures (up to a minor rescaling) may be interpreted as the rotation that transports the director frame from one segment to the next.

Consider the function ψ

$$\psi(t) = \frac{\arcsin(t/2)}{t/2} \quad \text{for } 0 \leqslant t \leqslant 2, \tag{2.15}$$

and note that $\psi(t) \approx 1$ for $t \ll 1$ (See the appendix for a plot of this function). Define the *adjusted deformation measure* to be

$$\omega_{i,J} = \psi(|\boldsymbol{\kappa}_i|)\, \boldsymbol{\kappa}_i \cdot \boldsymbol{e}_J. \tag{2.16}$$

This is well defined for all values of κ since $|\boldsymbol{\kappa}_i| = |q_i - \overline{q}_i| \leqslant 2\,|q_i| = 2$. This rescaling is insignificant in the continuum limit where $d^{i-1} \approx d^i$, $q_i \approx 1$ and $|\boldsymbol{\kappa}_i| \ll 1$, implying $\psi(|\boldsymbol{\kappa}_i|) \approx 1$. Even for moderate values of $|\boldsymbol{\kappa}_i|$, the original and adjusted deformations measures are not very different, $\omega_{i,J} \approx \boldsymbol{\kappa}_i \cdot \boldsymbol{e}_J$, as the variations of the function ψ are bounded by $1 \leqslant \psi(t) \leqslant \pi/2$.

The adjusted deformation measure has a simple geometric interpretation. We start from the decomposition (2.2) of the rotation gradient $q_i = r_{\boldsymbol{n}_i}(\theta_i) = \cos\frac{\theta_i}{2} + \boldsymbol{n}_i \sin\frac{\theta_i}{2} = \exp\frac{\boldsymbol{n}_i\,\theta_i}{2}$, where $\boldsymbol{n}_i$ is a unit vector aligned with the axis of the rotation q_i, and θ_i is the angle of this rotation, $0 \leqslant \theta \leqslant \pi$. In view of equation (2.13), $\boldsymbol{\kappa}_i = q_i - \overline{q}_i = 2\sin\frac{\theta_i}{2}\,\boldsymbol{n}_i$. In particular, $|\boldsymbol{\kappa}_i| = 2\sin\frac{\theta_i}{2}$ and so $\psi(|\boldsymbol{\kappa}_i|) = \frac{\theta_i/2}{\sin(\theta_i/2)}$ from equation (2.15). The adjusted strain is then $\omega_{i,J}\,\boldsymbol{e}_J = \psi(|\boldsymbol{\kappa}_i|)\,\boldsymbol{\kappa}_i = \frac{\theta_i/2}{\sin(\theta_i/2)}\,2\sin\frac{\theta_i}{2}\,\boldsymbol{n}_i = \theta_i\,\boldsymbol{n}_i$: in effect, the adjustment factor $\psi(|\boldsymbol{\kappa}_i|)$ transforms $\boldsymbol{\kappa}_i = 2\,\mathcal{I}(q_i)$ (twice the vector part of q_i) into $\omega_{i,J}\,\boldsymbol{e}_J = \theta_i\,\boldsymbol{n}_i = 2\log q_i$ (twice its logarithm).

Now, rewriting $q_i = \overline{d^{i-1}}\,d^i = \overline{d^{i-1}}\left(d^i\,\overline{d^{i-1}}\right)d^{i-1} = q_i^{\text{right}}$, one sees that q_i is conjugate to $d^i\,\overline{d^{i-1}}$. Combining with $q_i = \cos\frac{\theta_i}{2} + \boldsymbol{n}_i\sin\frac{\theta_i}{2}$, we have $d^i\,\overline{d^{i-1}} = d^{i-1}\,q_i\,\overline{d^{i-1}} = \cos\frac{\theta_i}{2} + (d^{i-1} * \boldsymbol{n}_i)\sin\frac{\theta_i}{2} = \exp\frac{(d^{i-1} * \boldsymbol{n}_i)\,\theta_i}{2}$: as is well known, the conjugate rotation $d^i\,\overline{d^{i-1}}$ has the same angle θ_i as the original rotation q_i and its axis is obtained by applying the rotation d^{i-1} to the original axis. This can be rewritten as

$$d^i = \exp\left(\frac{\boldsymbol{\Omega}_i}{2}\right) d^{i-1} \tag{2.17}$$

where $\boldsymbol{\Omega}_i = d^{i-1} * \boldsymbol{n}_i\,\theta_i = d^{i-1} * \omega_{i,J}\,\boldsymbol{e}_J = \omega_{i,J}\,\boldsymbol{d}^{i-1}_J$ is a (finite) rotation vector. Similar relations have been derived in the work of [27]. Repeating the same argument with $q_i = \overline{d^{i-1}}\,d^i = \overline{d^i}\,(d^i\,\overline{d^{i-1}})\,d^i = q_i^{\text{left}}$, one can show that the vector $\boldsymbol{\Omega}$ has the same decomposition in the other directors frame, $\boldsymbol{\Omega}_i = \omega_{i,J}\,\boldsymbol{d}^i_J$:

$$\boldsymbol{\Omega}_i = \omega_{i,J}\,\boldsymbol{d}^{i-1}_J = \omega_{i,J}\,\boldsymbol{d}^i_J. \tag{2.18}$$

Equations (2.17–2.18) show that *the adjusted deformation measures $\omega_{i,J}$ are the components of the rotation vector $\boldsymbol{\Omega}_i$ that maps one set of directors frame $(\boldsymbol{d}^{i-1}_I)_{I=1,2,3}$ to the other one $(\boldsymbol{d}^i_I)_{I=1,2,3}$* across the vertex $\boldsymbol{x}_i$. Remarkably, these components are identical in both the directors frame.

One could build a Discrete elastic rod model based on the adjusted deformation measure $\omega_{i,J}\,\boldsymbol{e}_J = 2\,\overline{d^{i-1}} * \log\left(d^i\,\overline{d^{i-1}}\right) = 2\,\overline{d^i} * \log\left(d^i\,\overline{d^{i-1}}\right)$ instead of the deformation measure $\boldsymbol{\kappa}_i$ proposed in section 2.6. The benefit is that $\omega_{i,J}$ have an even simpler interpretation, see equations (2.17–2.18). The drawback is that the function ψ gets involved in the calculation of the strain, resulting in cumbersome formulas for the strain gradients (Section 3). Therefore, we continue to use the original deformation measures.

3 Variations of the discrete deformation measures

In this section, we present explicit formulae for the first and second derivatives of the deformation measures $\boldsymbol{\kappa}_i$ (summarized in section 2.7) with respect to $\boldsymbol{X}$. The first gradient is required for determination of the internal forces, which are the first gradient of the strain energy. The availability of the second gradient in analytical form makes it possible to use implicit time-stepping methods (in dynamic problems) or to evaluate the Hessian for second order methods (in static problems).

Our notation for variations is first introduced based on a simple example. For a function $\boldsymbol{y} = \boldsymbol{f}(\boldsymbol{x})$ taking a vector argument $\boldsymbol{x}$ and returning a vector $\boldsymbol{y}$, the first variation is the linear mapping $\delta\boldsymbol{x} \mapsto \delta\boldsymbol{y} = \boldsymbol{f}'(\boldsymbol{x}) \cdot \delta\boldsymbol{x}$, where $\delta\boldsymbol{x}$ is a perturbation to $\boldsymbol{x}$ and $\boldsymbol{f}'(\boldsymbol{x})$ is the gradient matrix. To compute the second variation, we start from $\delta\boldsymbol{y} = \boldsymbol{f}'(\boldsymbol{x}) \cdot \delta\boldsymbol{x}$, perturb the argument $\boldsymbol{x}$ of $\boldsymbol{f}'$ as $\boldsymbol{x} + \delta\boldsymbol{x}$ and linearize the result as $\boldsymbol{f}'(\boldsymbol{x} + \delta\boldsymbol{x}) \cdot \delta\boldsymbol{x} \approx \boldsymbol{f}'(\boldsymbol{x}) \cdot \delta\boldsymbol{x} + \boldsymbol{f}''(\boldsymbol{x}) : (\delta\boldsymbol{x} \otimes \delta\boldsymbol{x})$. Here, the second variation is defined as the second order term $\delta^2\boldsymbol{y} := \boldsymbol{f}''(\boldsymbol{x}) : (\delta\boldsymbol{x} \otimes \delta\boldsymbol{x})$, where $\boldsymbol{f}''(\boldsymbol{x})$ is the Hessian. By construction, $\delta^2\boldsymbol{y}$ is a quadratic form of $\delta\boldsymbol{x}$.

In this section, the reference configuration is fixed and the degrees of freedom are perturbed by $\delta\boldsymbol{X} = (\cdots, \delta\boldsymbol{x}_i, \delta\varphi^i, \cdots)$. We simply present the final results; the detailed calculations are cumbersome but straightforward and provided in an appendix.

- **unit tangents** $\boldsymbol{t}^i = (\boldsymbol{x}_{i+1} - \boldsymbol{x}_i)/|\boldsymbol{x}_{i+1} - \boldsymbol{x}_i|$ from equation (2.6),

$$\begin{aligned} \delta\boldsymbol{t}^i &= \tfrac{\boldsymbol{I} - \boldsymbol{t}^i \otimes \boldsymbol{t}^i}{|\boldsymbol{x}_{i+1} - \boldsymbol{x}_i|} \cdot (\delta\boldsymbol{x}_{i+1} - \delta\boldsymbol{x}_i) \\ \delta^2\boldsymbol{t}^i &= -\tfrac{\boldsymbol{\tau}^i + (\boldsymbol{\tau}^i)^{T(132)} + (\boldsymbol{\tau}^i)^{T(231)}}{|\boldsymbol{x}_{i+1} - \boldsymbol{x}_i|^2} : ((\delta\boldsymbol{x}_{i+1} - \delta\boldsymbol{x}_i) \otimes (\delta\boldsymbol{x}_{i+1} - \delta\boldsymbol{x}_i)), \end{aligned} \tag{3.1}$$

  where $\boldsymbol{I}$ is the identity matrix, $\boldsymbol{\tau}^i$ is the third-order tensor $\boldsymbol{\tau}^i = (\boldsymbol{I} - \boldsymbol{t}^i \otimes \boldsymbol{t}^i) \otimes \boldsymbol{t}^i$, the colon denotes the double contraction of the *last* two indices of the rank-three tensor on the left-hand side. For any permutation (n_1, n_2, n_3) of $(1, 2, 3)$, $T(n_1, n_2, n_3)$ denotes a generalized transpose of a rank-three tensor such that $((\boldsymbol{\tau}^i)^{T(n_1,n_2,n_3)})_{i_1\, i_2\, i_3} = (\boldsymbol{\tau}_{i_{n_1}\, i_{n_2}\, i_{n_3}})$;

- **parallel transport** $p^i = p^{\boldsymbol{t}^i}_{\boldsymbol{T}^i}$ from equations (2.9) and (2.3),

$$\begin{aligned} \delta\hat{\boldsymbol{p}}^i &= \left((\boldsymbol{t}^i)_\times - \tfrac{\boldsymbol{t}^i \otimes \boldsymbol{k}^i}{2}\right) \cdot \delta\boldsymbol{t}^i \\ \delta^2\hat{\boldsymbol{p}}^i &= \left((\boldsymbol{t}^i)_\times - \tfrac{\boldsymbol{t}^i \otimes \boldsymbol{k}^i}{2}\right) \cdot \delta^2\boldsymbol{t}^i + \left(\delta\boldsymbol{t}^i \cdot \tfrac{\boldsymbol{k}^i \otimes \boldsymbol{T}^i + \boldsymbol{T}^i \otimes \boldsymbol{k}^i}{4\,(1 + \boldsymbol{T}^i \cdot \boldsymbol{t}^i)} \cdot \delta\boldsymbol{t}^i\right) \boldsymbol{t}^i - (\delta\boldsymbol{t}^i \otimes \delta\boldsymbol{t}^i) \cdot \tfrac{\boldsymbol{k}^i}{2} \end{aligned} \tag{3.2}$$

  where for any vector $\boldsymbol{a}$, $\boldsymbol{a}_\times$ is the linear operator

$$\boldsymbol{a}_\times : \boldsymbol{u} \mapsto \boldsymbol{a} \times \boldsymbol{u} \tag{3.3}$$

  and $\boldsymbol{k}^i$ is the binormal defined by

$$\boldsymbol{k}^i = \frac{2\,\boldsymbol{T}^i \times \boldsymbol{t}^i}{1 + \boldsymbol{T}^i \cdot \boldsymbol{t}^i}. \tag{3.4}$$

- **directors rotation** d^i from equation (2.8),

$$\begin{aligned} \delta\hat{\boldsymbol{d}}^i &= \delta\varphi^i \boldsymbol{t}^i + \delta\hat{\boldsymbol{p}}^i \\ \delta^2\hat{\boldsymbol{d}}^i &= \delta\varphi^i\, \delta\boldsymbol{t}^i + \delta^2\hat{\boldsymbol{p}}^i. \end{aligned} \tag{3.5}$$

- **rotation gradient** q_i from equation (2.11),

$$\begin{aligned} \delta\hat{\boldsymbol{q}}_i &= \overline{d^{i-1}} * (\delta\hat{\boldsymbol{d}}^i - \delta\hat{\boldsymbol{d}}^{i-1}) \\ \delta^2\hat{\boldsymbol{q}}_i &= \overline{d^{i-1}} * (\delta^2\hat{\boldsymbol{d}}^i - \delta^2\hat{\boldsymbol{d}}^{i-1}) + \delta\hat{\boldsymbol{q}}_i \times (\overline{d^{i-1}} * \delta\hat{\boldsymbol{d}}^{i-1}). \end{aligned} \tag{3.6}$$

- **discrete bending and twisting strain measure vector $\boldsymbol{\kappa}_i$** from equation (2.13),

$$\begin{array}{rcl} \delta\boldsymbol{\kappa}_i & = & \mathcal{I}\left(\delta\hat{\boldsymbol{q}}_i\, q_i\right) \\ \delta^2\boldsymbol{\kappa}_i & = & \mathcal{I}\left(\left(\delta^2\hat{\boldsymbol{q}}_i - \frac{\delta\hat{\boldsymbol{q}}_i\cdot\delta\hat{\boldsymbol{q}}_i}{2}\right) q_i\right) \end{array} \tag{3.7}$$

  where $\mathcal{I}(q) = \frac{q-\bar{q}}{2}$ denotes the vector part of a quaternion q.

- **stretching measure** ε^i from equation (2.14),

$$\begin{array}{rcl} \delta\varepsilon^i & = & \frac{\boldsymbol{x}_{i+1}-\boldsymbol{x}_i}{\ell}\cdot\left(\delta\boldsymbol{x}_{i+1}-\delta\boldsymbol{x}_i\right) \\ \delta^2\varepsilon^i & = & \frac{1}{\ell}\left(\delta\boldsymbol{x}_{i+1}-\delta\boldsymbol{x}_i\right)\cdot\left(\delta\boldsymbol{x}_{i+1}-\delta\boldsymbol{x}_i\right). \end{array} \tag{3.8}$$

In these formula, the first and second variations of the rotations p^i, d^i and q_i are not captured by quaternions but by regular *vectors*, bearing a hat, such as $\delta\hat{\boldsymbol{p}}^i$, $\delta^2\hat{\boldsymbol{p}}^i$, $\delta\hat{\boldsymbol{d}}^i$, etc. Equations (3.1–3.8) involve standard calculations from Euclidean geometry: the more advanced quaternion calculus is only required in the proof given in an appendix.

Equations (3.1–3.8) suffice to calculate the strain gradients numerically. They can be implemented easily and efficiently using standard libraries for vector and matrix algebra. Overall, the proposed method for calculating the strain gradients is simpler than that appearing in earlier work [12, 2, 30, 26].

In equations (3.1–3.8), the perturbations to the degrees of freedom such as $\delta\boldsymbol{x}_i$ and $\delta\varphi^i$ are dummy variables. The first-order variations such as $\delta\boldsymbol{t}^i$, $\delta\hat{\boldsymbol{p}}^i$, must be represented numerically as linear forms, by storing their coefficients as vectors. Similarly, the second-order variations such as $\delta^2\boldsymbol{t}^i$, $\delta^2\hat{\boldsymbol{p}}^i$, etc. are represented as quadratic forms, whose coefficients are stored as sparse symmetric matrices; for further details on this implementation aspects, the reader is referred to the related work of [26]. All these coefficients depend on the current configuration and must be updated whenever the degrees of freedom $\boldsymbol{X}$ or the reference configuration change.

These vectors and symmetric matrices should be stored at an appropriate place in the data structure representing the Discrete elastic rod. The tensors representing $\delta\boldsymbol{t}^i$, $\delta\hat{\boldsymbol{p}}^i$, $\delta^2\hat{\boldsymbol{p}}^i$ and $\delta^2\hat{\boldsymbol{d}}^i$ depend on the perturbations $\delta\boldsymbol{x}_i$ and $\delta\boldsymbol{x}_{i+1}$ to the nodes adjacent to a given segment, and therefore best stored in the data structure representing segments, which have access naturally to the degrees of freedom of the adjacent nodes. The quantities $\delta\hat{\boldsymbol{d}}^i$ and $\delta^2\hat{\boldsymbol{d}}^i$ make use the twisting angle $\delta\varphi^i$ in addition to the adjacent nodes $\delta\boldsymbol{x}_i$ and $\delta\boldsymbol{x}_{i+1}$, and should be stored in the data structure representing the material frame attached to particular segment. The quantities $\delta\hat{\boldsymbol{q}}_i$, $\delta\boldsymbol{\kappa}_i$, $\delta^2\hat{\boldsymbol{q}}_i$ and $\delta^2\boldsymbol{\kappa}_i$ are best stored in a data structure representing an elastic hinge at a node, that depends on the material frames at the adjacent segments.

4 Constitutive models

The discrete kinematics from sections 2 and 3 can be combined with a variety of constitutive laws to produce discrete numerical models for rods that are elastic, viscous, visco-elastic, etc.: the procedure has been documented in previous work, and it is similar to the general approach used in finite-element analysis. Elastic problems are treated by introducing a strain energy function $U(\boldsymbol{X})$ whose gradient with respect to $\boldsymbol{X}$ yields minus the discrete elastic forces [12, 26], viscous problems are treated by introducing a discrete Rayleigh potential $U(\boldsymbol{X}, \dot{\boldsymbol{X}})$ whose gradient with respect to velocities $\dot{\boldsymbol{X}}$ yields discrete viscous forces [11, 14, 2]. More advanced constitutive models such as visco-elastic laws can be treated by variational constitutive updates of a discrete potential that makes use of the same discrete deformation measures [26]. In [26], it is emphasized that these different constitutive models can be implemented *independently* of the geometric definition of discrete deformation measure. Using this decoupled approach, it is straightforward to combine the kinematic element proposed in the present work with constitutive element from previous work. We illustrate this with the classical, linearly elastic rod in section 4.1 (Kirchhoff rod model), and a discrete inextensible ribbon model in section 4.2 (Wunderlich model). The latter is a novel application of the Discrete elastic rod method.

4.1 Elastic rods (Kirchhoff model)

The classical, continuous theory of elastic rods uses a strain energy functional $U[\boldsymbol{\kappa}] = \int_0^L E(\kappa_{(1)}(s), \kappa_{(2)}(s), \kappa_{(3)}(s))\,\mathrm{d}s$, where $\kappa_{(I)}(s) = \boldsymbol{\kappa}(s)\cdot\boldsymbol{d}_I(s)$ are the components of the rotation gradient in the frame of directors, see equation (1.3). For an inextensible, linearly elastic rod made of a Hookean material with natural curvature $\kappa_{(0)}$, for instance, the strain energy density is

$$E(\kappa_{(1)}(s), \kappa_{(2)}(s), \kappa_{(3)}(s)) = \frac{1}{2}\,Y\,I_1\,\kappa_{(1)}^2 + \frac{1}{2}\,Y\,I_2\,(\kappa_{(2)} - \kappa_{(0)})^2 + \frac{1}{2}\,\mu\,J\,\kappa_{(3)}^2 \tag{4.1}$$

where Y and μ are the Young modulus and the shear modulus of the material, I_1 and I_2 are the geometric moments of inertia of the cross-section, and J is the torsional constant.

In the discrete setting, we introduce a strain energy $\sum_i E_i(\boldsymbol{\kappa}_i)$ where the sum runs over all interior nodes i. The strain energy assigned to an interior node i is defined in terms of the strain energy density as

$$E_i(\boldsymbol{\kappa}_i) = \ell\,E\left(\frac{\boldsymbol{\kappa}_i}{\ell}\right), \tag{4.2}$$

(no implicit sum over i), where ℓ is the undeformed length of the segments for a uniform mesh. The factor ℓ in the argument of E takes care of the fact that $\boldsymbol{\kappa}_i$ is an integrated quantity, *i.e.*, it is $\frac{\boldsymbol{\kappa}_i}{\ell}\cdot\boldsymbol{e}_J$ and not just $\boldsymbol{\kappa}_i\cdot\boldsymbol{e}_J$ that converges to the continuous strain $\kappa_{(J)}(s)$; for a non-uniform grid, this ℓ would need to be replaced with the Voronoi length associated with the interior vertex i in undeformed configuration. The factor ℓ in factor of E in equation (4.2) warrants [12] that the discrete sum $\sum_i E_i = \sum_i \ell\,E$ converges to the integral $\int_0^L E\,\mathrm{d}s = U$.

Consider for instance an equilibrium problem with dead forces $\boldsymbol{F}_i$ on the nodes: it is governed by the total potential energy $\Phi(\boldsymbol{X})$ defined in terms of $\boldsymbol{X} = (\boldsymbol{x}_0, \varphi_0, \ldots, \varphi_{N-1}, \boldsymbol{x}_N)$ as

$$\Phi(\boldsymbol{X}) = \sum_{i=1}^{N-1} E_i(\boldsymbol{\kappa}_i(\boldsymbol{x}_{i-1}, \varphi^{i-1}, \boldsymbol{x}_i, \varphi^i, \boldsymbol{x}_{i+1})) - \sum_{i=0}^{N} \boldsymbol{F}_i\cdot\boldsymbol{x}_i. \tag{4.3}$$

This energy is minimized subject to the inextensibility constraints

$$\forall i \in (0, N-1) \qquad \varepsilon^j(\boldsymbol{x}_j, \boldsymbol{x}_{j+1}) = 0. \tag{4.4}$$

In equations (4.3–4.4), the elastic deformation measures $\boldsymbol{\kappa}_i$ and ε^j is reconstructed in terms of the unknown $\boldsymbol{X}$ by the method described in section 2, as expressed by the notation $\boldsymbol{\kappa}_i(\boldsymbol{x}_{i-1}, \varphi^{i-1}, \boldsymbol{x}_i, \varphi^i, \boldsymbol{x}_{i+1})$ and $\varepsilon^j(\boldsymbol{x}_j, \boldsymbol{x}_{j+1})$.

In the case of dead forces, the first and second variations of the total potential energy is derived as

$$\begin{aligned} \delta\Phi &= \textstyle\sum_{i=1}^{N-2} \dfrac{\partial E_i}{\partial \boldsymbol{\kappa}_i}\cdot\delta\boldsymbol{\kappa}_i - \sum_{i=0}^{N-1} \boldsymbol{F}_i\cdot\delta\boldsymbol{x}_i \\ \delta^2\Phi &= \textstyle\sum_{i=1}^{N-2} \left(\delta\boldsymbol{\kappa}_i\cdot\dfrac{\partial^2 E_i}{\partial \boldsymbol{\kappa}_i^2}\cdot\delta\boldsymbol{\kappa}_i + \dfrac{\partial E_i}{\partial \boldsymbol{\kappa}_i} : \delta^2\boldsymbol{\kappa}_i\right), \end{aligned} \tag{4.5}$$

see for instance [26]. Here, $\frac{\partial E_i}{\partial \boldsymbol{\kappa}_i}$ and $\frac{\partial^2 E_i}{\partial \boldsymbol{\kappa}_i^2}$ are the internal stress and tangent elastic stiffness produced by the elastic constitutive model $E_i(\boldsymbol{\kappa}_i)$. The two terms appearing in the parentheses in the right-hand side of $\delta^2\Phi$ are known as the elastic and geometric stiffness, respectively. The first and second variations of the strain, $\delta\boldsymbol{\kappa}_i$ and $\delta^2\boldsymbol{\kappa}_i$, are available from section 3: the equilibrium can be solved using numerical methods that require evaluations of the Hessian of the energy. Note that the Hessian can be represented as a sparse matrix thanks to the local nature of the energy contributions $E_i(\boldsymbol{\kappa}_i(\boldsymbol{x}_{i-1}, \varphi^{i-1}, \boldsymbol{x}_i, \varphi^i, \boldsymbol{x}_{i+1}))$ in equation (4.3).

For the applications presented in the forthcoming sections, we have minimized $\Phi(\boldsymbol{X})$ in equation (4.3) using the sequential quadratic programming method (SQP) described by [29]; it is an extension of the Newton method for non-linear optimization problems which can handle the non-linear constraints in equation (4.4). It requires the evaluation of the first and second gradient of the energy Φ, see equation (4.5), and of the first gradient of the constraints that are available from equation (3.8). We used an in-house implementation of the SQP method in the `C++` language, with matrix inversion done using the `SimplicialLDLT` method available from the Eigen library [23].

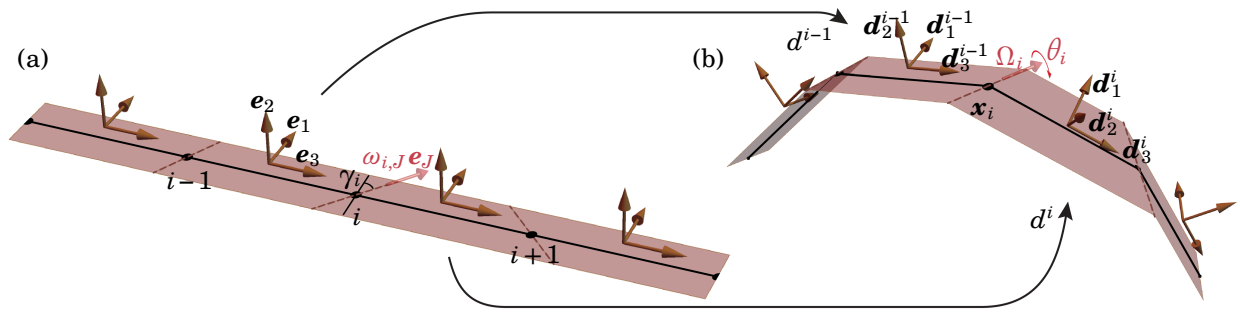

Figure 4.1: A discrete inextensible ribbon: (a) flat configuration and (b) current (folded) configuration obtained by folding along the generatrices (brown dashed lines) by an angle θ_i. By the inextensibility condition, the fold line through vertex $\boldsymbol{x}_i$ in current configuration lies at the intersection of the adjacent faces, *i.e.*, of the planes spanned by $\boldsymbol{d}_1^{i-1}$ and $\boldsymbol{d}_3^{i-1}$ on the one hand and by $\boldsymbol{d}_1^i$ and $\boldsymbol{d}_3^i$ on the other hand.

4.2 Inextensible elastic ribbons (Wunderlich model)

Ribbons made up of material that are sensitive to light [41, 22] or temperature change [8] have been used to design lightweight structures that can be actuated. They are easy to fabricate, typically by cutting out a thin sheet of material, and their thin geometry can turn the small strains produced by actuation into large-amplitude motion. For this reason, there has been a surge of interest towards mechanical models for elastic ribbons recently. When the width-to-thickness ratio of a ribbon cross-section is sufficiently large, its mid-surface is effectively inextensible. Sadowsky has proposed a one-dimensional mechanical model for inextensible ribbons [33]. Sadowsky model is one-dimensional but differs from classical rod models in two aspects: one of the two bending modes is inhibited due to the large width-to-thickness aspect-ratio, and the two remaining twisting and bending modes are governed by an *non-quadratic* strain energy potential that effectively captures the inextensible deformations of the ribbon mid-surface. Sadowsky's strain energy is non-convex which can lead to the formation of non-smooth solution representing a micro-structure [20, 31]; to avoid these difficulties, we use the higher-order model of Wunderlich that accounts for the dependence of the energy on the longitudinal gradient of bending and twisting strain [40].

The Wunderlich model has been solved numerically by a continuation method, see for instance the work of [37]. The continuation method is an extension of the shooting method that can efficiently track solutions depending on a parameter [19]. It requires the full boundary-value problem of equilibrium to be specified spelled out, which is quite impractical in the case of Wunderlich ribbons. A recent and promising alternative is the high-order method of [16] that starts from linear and quadratic interpolations of the bending and twisting strains, and treats the center-line position and the directors as secondary (reconstructed) quantities. In the present work, we explore an alternative approach, and show that simulations of the Wunderlich model are possible with limited additional work on top of the generic Discrete elastic rod framework.

We build up on the work of [18] who have shown that the Wunderlich model can be viewed as a special type of a non-linear elastic rod, see also [36]. Accordingly, simulations of the Wunderlich model can be achieved using a simple extension of the Discrete elastic rod model, which we describe now. We first introduce a geometric model for a *discrete inextensible ribbon*, in which the inextensibility of the mid-surface is fully taken into account. We start from a rectangular strip lying in the plane spanned by $(\boldsymbol{e}_1, \boldsymbol{e}_3)$, as shown in figure 4.1a. Through every node (shown as black dots in the figure), we pick a folding direction within the plane of the strip (brown dotted line in the figure); we denote by $\pi/2 - \gamma_i$ the angle of the fold line relative to the centerline. Next, we fold along each one of these lines by an angle θ_i, as shown in figure 4.1b. We call a discrete inextensible ribbon the resulting surface. By construction, it is isometric to the original strip.

Let us now introduce the director frames $\boldsymbol{d}_I^i$ following rigidly each one of the faces: the planar faces are spanned by the directors $\boldsymbol{d}_1^i$ and $\boldsymbol{d}_3^i$. By construction the vector $\boldsymbol{\Omega}_i$ for the rotation that maps one frame, $\boldsymbol{d}_I^{i-1}$, to the next, $\boldsymbol{d}_I^i$, see equation (2.17), is aligned with the fold line. We observe that the unit tangent

along the fold direction is $\boldsymbol{e}_3 \sin\gamma_i + \boldsymbol{e}_1 \cos\gamma_i$ in the flat configuration of the strip; it is therefore mapped to $\boldsymbol{d}_3^{i-1} \sin\gamma_i + \boldsymbol{d}_1^{i-1} \cos\gamma_i = \boldsymbol{d}_3^{i} \sin\gamma_i + \boldsymbol{d}_1^{i} \cos\gamma_i$ in the current configuration. In view of this, we conclude

$$\boldsymbol{\Omega}_i = \left(\boldsymbol{d}_3^{i-1} \sin\gamma_i + \boldsymbol{d}_1^{i-1} \cos\gamma_i\right) \theta_i = \left(\boldsymbol{d}_3^{i} \sin\gamma_i + \boldsymbol{d}_1^{i} \cos\gamma_i\right) \theta_i.$$

Comparing with equation (2.18), we obtain the discrete deformation measure in the developable ribbon as $\omega_{i,1} = \theta_i \cos\gamma_i$ (bending mode), $\omega_{i,2} = 0$ (inhibited bending mode) and $\omega_{3,i} = 0$ (twisting mode). Eliminating θ_i, we find $\omega_{i,2} = 0$ and $\frac{\omega_{i,3}}{\omega_{i,1}} = \tan\gamma_i$, which can be rewritten in terms of the original discrete strain $\boldsymbol{\kappa}_i = (\kappa_{i,1}, \kappa_{i,2}, \kappa_{i,3})$ with the help of equation (2.15) as

$$\begin{aligned} \kappa_{i,2} &= 0 \\ \kappa_{i,3} &= \eta_i \, \kappa_{i,1} \end{aligned} \tag{4.6}$$

where

$$\eta_i = \tan\gamma_i.$$

The continuous version of the developability conditions is $\kappa_2(s) = 0$ and $\kappa_3(s) = \eta(s)\,\kappa_1(s)$, where $\eta(s) = \tan\gamma(s)$ and $\pi/2 - \gamma(s)$ is the angle between the generatrix and the tangent, see for instance [18]. It is remarkable that the discrete developability conditions (4.6) are strictly identical. This is a consequence of the simple geometric interpretation for the discrete deformation measures introduced in section 2.

To simulate inextensible ribbons, we introduce the unknown η_i as an additional degree of freedom at each one of the interior nodes, and we use in equation (4.3) a strain energy density directly inspired from that of Wunderlich [18, 37]

$$E_i(\boldsymbol{\kappa}_i, \eta_{i-1}, \eta_i, \eta_{i+1}) = \frac{D\,w}{2\,\ell} \kappa_{i,1}^2 \, (1+\eta_i^2)^2 \, \frac{1}{w\,\eta_i'} \, \ln\left(\frac{1+\frac{1}{2}\,\eta_i'\,w}{1-\frac{1}{2}\,\eta_i'\,w}\right). \tag{4.7}$$

In equation (4.7), $D = \frac{Y\,h^3}{12\,(1-\nu^2)}$ is the bending modulus from plate theory, h is the thickness, w is the width and ℓ is the discretization length. The quantity η_i' is calculated by a central-difference approximation of the gradient of η,

$$\eta_i' = \frac{\eta_{i+1} - \eta_{i-1}}{2\,\ell},$$

where ℓ is the mesh size.

The discrete potential energy $\Phi(\boldsymbol{X})$ is minimized by the same numerical method as described in section 4.1, taking into account the kinematic constraints (4.6) and the centerline inextensibility constraints (4.4).

5 Illustrations

In this section, the Discrete elastic rod model is used to simulate

- a linearly elastic model for an isotropic beam, §5.1,
- a linearly elastic model for an anisotropic beam with natural curvature, §5.2,
- Sano and Wada's extensible ribbon model, §5.3,
- Wunderlich's inextensible ribbon model, §5.4.

These examples serve to illustrate the capabilities of the model. In addition, comparison with reference solutions available from the literature provide a verification of its predictions.

5.1 Euler buckling

We consider Euler buckling for a planar, inextensible elastic rod that is clamped at one endpoint. We consider two types of loading: either a point-like force f_p at the endpoint opposite to the clamp, or a force f_d distributed along the length of the rod. In both cases, the force is applied along the initial axis of the rod, is invariable (dead loading), and is counted positive when compressive. A sketch is provided in figure 5.1.

Mathematically, the equilibria of the rod having bending modulus B are the stationary points of the functional $\Phi = \int_0^L \frac{B}{2}\,\theta'^2(s)\,\mathrm{d}s + f_\mathrm{p}\,x(L)$ (point-like loading) or $\Phi = \int_0^L \left(\frac{B}{2}\,\theta'^2(s) + f_\mathrm{d}\,x(s)\right)\mathrm{d}s$ (distributed loading), subject to the clamping condition $\theta(0) = 0$. The coordinates of a point on the centerline $(x(s), y(s))$ are reconstructed using the inextensibility condition as $x(s)\,\boldsymbol{e}_1 + y(s)\,\boldsymbol{e}_2 = \int_0^s (\cos\theta\,\boldsymbol{e}_1 + \sin\theta\,\boldsymbol{e}_2)\,\mathrm{d}s$.

The boundary-value equilibrium problem for the Elastica is obtained by the Euler-Lagrange method as

$$0 = B\,\theta''(s) + \sin\theta(s) \times \begin{cases} f_\mathrm{p} & \text{(point-like load)} \\ f_\mathrm{d}\,(L-s) & \text{(distributed load)} \end{cases} \qquad \theta(0) = 0 \qquad \theta'(L) = 0. \tag{5.1}$$

By writing this problem in dimensionless form, one can effectively set the bending modulus, the length and the load to $B = 1$, $L = 1$, and $f_\mathrm{p} = \overline{f}_\mathrm{p}$ (point-like load) or $f_\mathrm{d} = \overline{f}_\mathrm{d}$ (distributed load), where the dimensionless load is

$$\overline{f}_\mathrm{p} = \frac{f_\mathrm{p}}{B/L^2} \qquad \overline{f}_\mathrm{d} = \frac{L\,f_\mathrm{d}}{B/L^2}. \tag{5.2}$$

The critical buckling loads are found by solving the *linearized* version of the buckling problem (5.1) (linear bifurcation analysis),

$$\begin{array}{lcll} \left(\overline{f}_\mathrm{p}\right)_\mathrm{crit} & = & \frac{\pi^2}{4} & \text{(point-like load)} \\ \left(\overline{f}_\mathrm{d}\right)_\mathrm{crit} & = & 7.837 & \text{(distributed load)} \end{array} \tag{5.3}$$

Numerical simulations of this Euler buckling problem are conducted using the Discrete elastic rod method, as explained in section 4.3. Simulations are set up with $B = 1$, $L = 1$, number of nodes $N = 100$. In view of this we expect to the buckling loads to be $f_\mathrm{d} = \overline{f}_\mathrm{d}$ $f_\mathrm{p} = \overline{f}_\mathrm{p}$. The inextensibility constraint is enforced exactly using SQP. Recall that the clamped boundary is enforced by fixing the first and second nodes as well as the first frame.

The typical simulation time is about 1/10s for each equilibrium on a personal computer, and the results are shown in figure 5.1, and compared to that obtained by solving (5.1) using the `bvp4c` solver from Matlab. A good agreement on the position of the endpoint of the rod is found in the entire post-bifurcation regime. In addition, the onset of bifurcation agrees accurately with the prediction (5.3) from the linear stability analysis.

5.2 Folding of an over-curved ring

A circular elastic ring with length L can buckle out of plane if its natural natural curvature $\kappa_{(0)}$ does not match the curvature $2\pi/L$ of the circle with length L. In the case of an over-curved ring, such that $\kappa_{(0)} > 2\,\pi/L$, a buckled shape featuring two symmetric lobes has been reported [28, 8, 7]. Here, we simulate the buckling of over-curved rings using the Discrete elastic rod model and compare the results to the experimental shapes reported by [28].

In the experiments of [28], a commercial slinky spring with a width $w = 5$ mm, thickness $t = 2$ mm and length $L = 314$ mm is used; Poisson's ratio has been measured as $\nu = 0.41$. Note that the aspect-ratio $t/w = 0.4$ is not small. In our simulations, we use a discrete version of the quadratic strain energy for a linearly elastic rod having an anisotropic cross-section ($I_1 \neq I_2$), see equations (4.1–4.3). We use the elastic moduli reported in the supplement of [28]:

$$Y\,I_1 = Y\,\frac{w\,t^3}{12} \qquad Y\,I_2 = Y\,\frac{w^3\,t}{12} \qquad \mu\,J = Y\,\frac{0.256\,w\,t^3}{2\,(1+\nu)}. \tag{5.4}$$

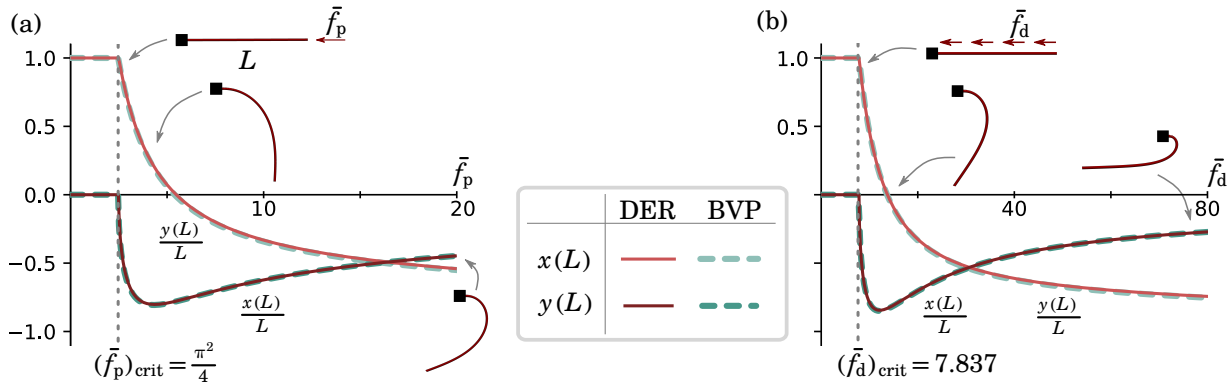

Figure 5.1: Buckling of a planar Elastica subject to (a) a point-like force applied at the endpoint and (b) a distributed force. Comparison of the solutions of the boundary-value problem (5.1) by a numerical shooting method (dashed curves) and of the Discrete elastic rod method (solid curves): the scaled coordinates of the endpoint $s = L$ are plotted as a function of the dimensionless load. The dotted vertical line is the first critical load predicted by a linear bifurcation analysis from equation (5.3).

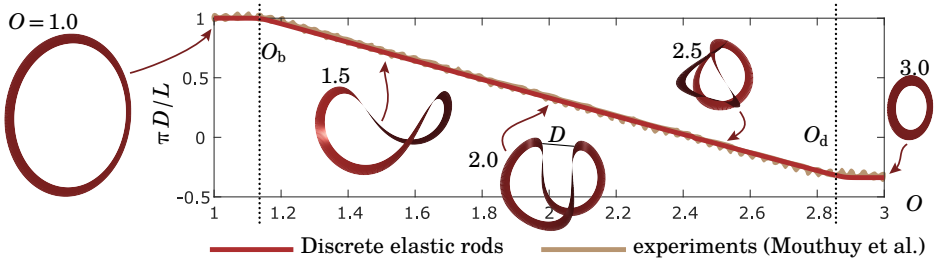

Figure 5.2: Equilibrium of an over-curved elastic ring. Material and geometric parameters correspond to the slinky used by [28] (see main text for values). a) Equilibrium configurations for different values of the over-curvature ratio O. b) Minimal distance of approach D as a function of O: comparison of Discrete elastic rod simulations and experiments [28]. The simulations reproduces both the initial buckling at O_b, and the 'de-buckling' into a flat, triply covered ring at O_d.

The value 0.256 in the numerator was obtained by [28] from the book of [39], and applies to the particular commercial Slinky used in their experiments. In the absence of applied loading, the value of the Young modulus is irrelevant and we set $Y = 1$ in the simulations.

The equilibria of the Discrete elastic rod are calculated numerically for different values of the dimensionless loading parameter $O = 2\,\pi\,\kappa_{(0)}/L$, with $O > 1$ corresponding to the over-curved case. We use $N = 400$ nodes. We start from a circular configuration having curvature $\kappa_{(0)} = 2\,\pi/L$. The Discrete elastic rod model is closed into a ring as follows: the first two nodes and the last two nodes are prescribed to $\boldsymbol{x}_0 = \boldsymbol{x}_{N-1} = \boldsymbol{0}$ and $\boldsymbol{x}_1 = \boldsymbol{x}_N = \ell\,\boldsymbol{e}_x$, respectively; the first and last frames are also fixed, such that $\boldsymbol{d}_1^0 = \boldsymbol{d}_1^{N-1} = \boldsymbol{e}_y$. Next, the over-curvature $\kappa_{(0)}$ is varied incrementally. For each value of $\kappa_{(0)}$, an equilibrium configuration is sought, and we extract the minimal distance D between pairs of opposite points on the ring. In figure 5.2, the scaled distance D is plotted as a function of O. A good agreement is found with the experiments over the entire range of values of the over-curvature parameter $O > 1$. The simulations correctly predict a planar, triply covered circular solution for $O > O_d \approx 2.85$, as seen in the experiments.

5.3 Buckling of a bent and twisted ribbon

We now turn to an effective rod model applicable to thin ribbons. Sano and Wada [34] have proposed an effective beam model that accounts for the stretchability of the ribbon having moderate width, thereby improving on Sadowsky's inextensibility assumption. A discrete version of their continuous model is of the form (4.3) with a strain energy per elastic hinge

$$E_i(\kappa_1, \kappa_2, \kappa_3) = \frac{1}{2\,\ell}\left(A_1\,\kappa_1^2 + A_2\left(\kappa_2^2 + \frac{\kappa_3^4}{\ell^2/\xi^2 + \kappa_2^2}\right) + A_3\,\kappa_3^2\right). \tag{5.5}$$

Here, ℓ is the uniform segment length in undeformed configuration, $A_1 = Y\,h\,w^3/12$ and $A_2 = Y\,h^3\,w/12$ are the initial bending moduli, $A_3 = Y\,h^3\,w/[6\,(1+\nu)]$ is the initial twisting modulus and $\xi^2 = (1-\nu^2)\,w^4/60\,h^2$. The parameter ξ is the typical length-scale where the stretchability of the mid-surface starts to play a role. The potential E_i from equation (5.5) is non-quadratic, meaning that the equivalent rod has non-linear elastic constitutive laws.

The elastic model (5.5) of Sano and Wada is applicable to thin ribbons, for $w \gg h$. It is based on kinematic approximations. A refined version of their model has been obtained recently by [5], by asymptotic expansion starting from shell theory; in the latter work, a detailed discussion of the validity of the various models for thin ribbons can also be found.

Following [34], we consider the buckling of a ribbon with length $L = \pi\,R$ bent into half a circle, whose ends are twisted in an opposite senses by an angle ϕ, see figure 5.3. Specifically, they identified a snapping instability which occurs for moderately wide ribbons, when the width $w < w^*$ is below a threshold $w^* \approx 1.24\sqrt{L\,h}$, but not for wider ribbons, when $w > w^*$; they showed that their equivalent rod model can reproduce this instability, as well as its disappearance for larger widths. In Figure 5.3, we compare the predictions of a Discrete elastic rod model using (5.5) with the original experiments and simulations from [34]. Our simulations use $N = 350$ vertices each. Our simulation results are in close agreement with both their experimental and numerical results. In particular, we recover the instability when $w < w^*$ only.

5.4 The elastic Möbius band

An extension of the Discrete elastic rod model that simulates the inextensible ribbon model of Wunderlich has been described in section 4.2, see equation (4.7). With the aim to illustrate and verify this discrete model, we simulate the equilibrium of a Möbius ribbon, and compare the results to those reported in the seminal paper of Starostin and van der Heijden [35]. In our simulations, the inextensible strip is first bent into a circle, and the endpoints are turned progressively twisted by an angle of 180° to provide the correct topology. The final equilibrium shapes are then recorded for all possible values of the aspect-ratio w/L. For these final equilibrium shapes, the conditions $\boldsymbol{x}_0 = \boldsymbol{x}_{N-1} = \boldsymbol{0}$ and $\boldsymbol{x}_1 = \boldsymbol{x}_N = \ell\,\boldsymbol{e}_x$ hold as earlier, and the orientation of the terminal material frames are such that $\boldsymbol{d}_1^0 = +\boldsymbol{e}_y$ and $\boldsymbol{d}_1^{N-1} = -\boldsymbol{e}_y$.

The equilibrium shape for a particular aspect-ratio $w/L = 1/\,(2\,\pi)$ is shown in figure 5.4a, with arc-length $L = 1$, width $w = 1/\,(2\,\pi)$ and $N = 150$ simulation nodes. A detailed comparison with the results of [35] is provided in figure 5.4b, where the scaled bending and twisting strains $\kappa_{i,1}/\ell$ and $\kappa_{i,3}/\ell$ from the discrete model with $N = 250$ vertices are compared to the strains $\kappa_1(s)$ and $\kappa_3(s)$ obtained by [35] using numerical shooting, for different values of the width w.

6 Conclusion

We have presented a new formulation of the Discrete elastic rod model. The formulation is concise and uses only the minimally necessary degrees of freedom: the position of the nodes and the angle of twist of the segments between the nodes. It naturally incorporates the adaptation condition without the need for any constraint, penalty or Lagrange multiplier. The resulting bending, twist and stretching deformation measures are consistent with their continuum counterparts, and have a natural physical interpretation in the discrete setting. Consequently, the formulation is versatile in the sense that it can be combined with a

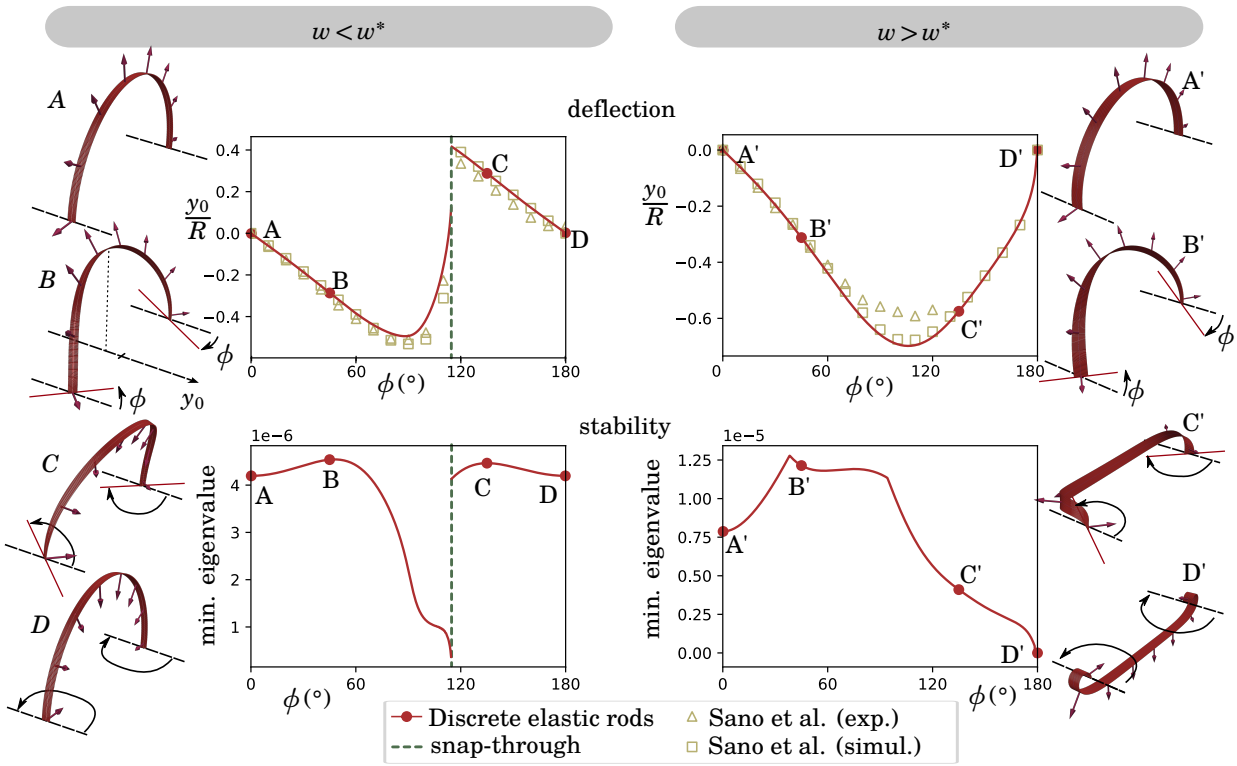

Figure 5.3: Equilibria of an extensible ribbon, as captured by Sano and Wada's equivalent rod model, see equation (5.5). *Top row*: equilibrium diagram showing the scaled value of the deflection y_0 at the center of the ribbon as a function of the twisting angle ϕ at the endpoints. Comparison of the experiments (triangles) and simulations (squares) from [34] with simulations using the Discrete elastic rod model (solid curves and circles). *Left column*: moderately wide ribbon $(h, w, R) = (0.2, 8, 108)$mm showing a snapping instability; *Right column*: wider ribbon $(h, w, R) = (0.2, 15, 108)$mm, in which the instability is suppressed. *Bottom row*: smallest eigenvalues of the tangent stiffness matrix, on the same solution branch shown as shown in the plot immediately above: the presence of an instability for $w < w^*$ (left column) is confirmed by the fact that the smallest eigenvalue reaches zero when the instability sets in.

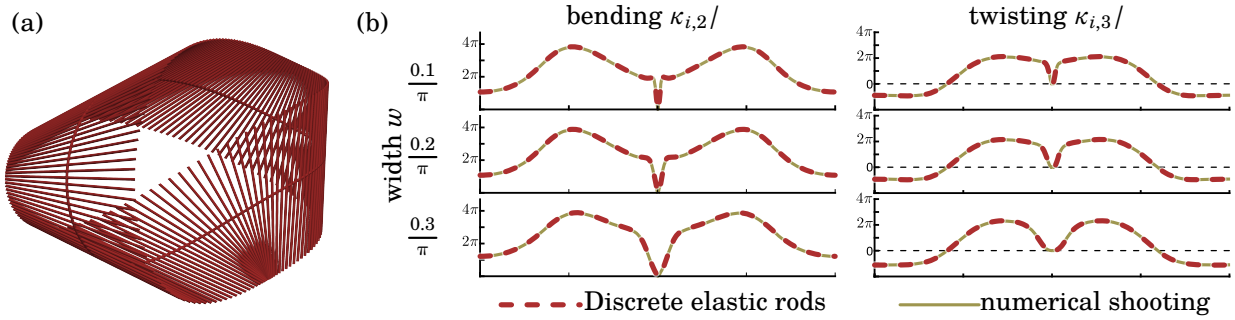

Figure 5.4: Simulation of an inextensible Möbius strip with $L = 1$. (a) Equilibrium width $w = 1/(2\pi)$, as simulated by the Discrete elastic rod model from section 4.2 with $N = 150$ nodes. (b) Distribution of bending and twisting: Discrete elastic rod simulations with $N = 250$ vertices (dashed curves) versus solution of [35] obtained by numerical shooting (solid curves); the latter have been properly rescaled to reflect our conventions.

variety of linear and nonlinear as well as elastic and inelastic constitutive relations. In fact, ribbons can be incorporated as generalized rods with a nonlinear constitutive model. Similarly, the formulation can be used both for static and dynamic simulations.

We have presented explicit formulae for the first and second derivatives of the deformation measures that eases implementation. We have demonstrated our method with four examples, and verified our results against prior experimental and theoretical findings in the literature.

The source code used for the numerical simulation is available through CaltechDATA at `https://data.caltech.edu/records/2024`.

All three authors conceived of the work and the formulation. KK conducted the theoretical and numerical calculations with advice from BA and KB. KK and BA took the lead in writing the manuscript and all three authors finalized it.

The authors declare that there are no competing interests.

The work began when BA visited Caltech as a Moore Distinguished Scholar. KK and KB gratefully acknowledge the support of the US Office of Naval Research through Multi-investigator University Research Initiative Grant ONR N00014-18-1-2624.

Appendices

A Plot of function ψ

The function $\psi(t)$ from equation (2.15) is plotted in figure A.1.

B Detailed derivation of the strain gradients

In this appendix, we provide a detailed derivation of the first and second gradients of the strain appearing in section 3.

To derive the first gradient, we continue to use the conventions of section 3: we use a perturbation $\delta\boldsymbol{X}$ of the degrees of freedom, and we denote by $\delta\boldsymbol{y} = \boldsymbol{f}'(\boldsymbol{x}) \cdot \delta\boldsymbol{x}$ the first variation of a generic quantity $\boldsymbol{y} = \boldsymbol{f}(\boldsymbol{x})$ entering in the reconstruction of the discrete strain, where $\boldsymbol{x}$ depends indirectly on the degrees of freedom $\boldsymbol{X}$.

For the second variation, however, we work here in a slightly more general setting than in the main text, as we consider two *independent* perturbations $\delta_1\boldsymbol{X}$ and $\delta_2\boldsymbol{X}$ of the degrees of freedom. We denote by $\delta_1\boldsymbol{x}$ and $\delta_2\boldsymbol{x}$ the corresponding perturbations to the variable $\boldsymbol{x}$, and by $\delta_1\boldsymbol{y}$ and $\delta_2\boldsymbol{y}$ the first-order variations of the functions: $\delta_1\boldsymbol{y} = \boldsymbol{f}'(\boldsymbol{x}) \cdot \delta_1\boldsymbol{x}$ and $\delta_2\boldsymbol{y} = \boldsymbol{f}'(\boldsymbol{x}) \cdot \delta_2\boldsymbol{x}$ are simply obtained by replacing the generic increment $\delta\boldsymbol{x}$ appearing in the first order variation $\delta\boldsymbol{y}$ with $\delta_1\boldsymbol{x}$ and $\delta_2\boldsymbol{x}$, respectively. To obtain the second variation, we perturb the argument $\boldsymbol{x}$ appearing in $\delta_1\boldsymbol{y} = \boldsymbol{f}'(\boldsymbol{x}) \cdot \delta_1\boldsymbol{x}$ as $\boldsymbol{x} + \delta_2\boldsymbol{x}$, leaving $\delta_1\boldsymbol{x}$ untouched,

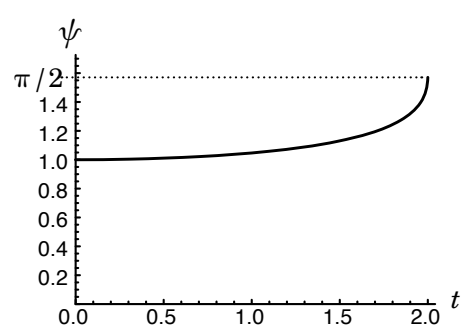

Figure A.1: Function $\psi(t)$ from equation (2.15) used to adjust the norm of the strain $\boldsymbol{\kappa}_i$ with $t = |\boldsymbol{\kappa}_i|$, see equation (2.16).

and we expand the result to first order in $\delta_2 \boldsymbol{x}$. This yields a quantity denoted as $\delta_{12}\boldsymbol{y}$, which we can write formally as $\delta_{12}\boldsymbol{y} = \boldsymbol{f}''(\boldsymbol{x}) : (\delta_1 \boldsymbol{x} \otimes \delta_2 \boldsymbol{x})$, where $\boldsymbol{f}''(\boldsymbol{x})$ is the Hessian. By a classical result in the calculus of variations, the quantity $\delta_{12}\boldsymbol{y}$ is bilinear and symmetric with respect to $\delta_1 \boldsymbol{x}$ and $\delta_2 \boldsymbol{x}$. The second variation $\delta^2 \boldsymbol{y}$ given in the main text is the quadratic form obtained by ultimately condensing the variations $\delta_1 \boldsymbol{x}$ and $\delta_2 \boldsymbol{x}$ appearing in $\delta_{12}\boldsymbol{y}$ into a single perturbation $\delta \boldsymbol{x} = \delta_1 \boldsymbol{x} = \delta_2 \boldsymbol{x}$.

B.1 Infinitesimal rotation vectors

As an important preliminary result, we show that the first variation of a rotation represented by a unit quaternion s can be characterized by means of first-order *vector-valued* increment $\delta \hat{\boldsymbol{s}} \in \mathbb{R}^3$, and that the second variation of s can be represented by means of a second-order *vector-valued* increment $\delta_{12}\hat{\boldsymbol{s}} \in \mathbb{R}^3$. These vectors will be referred as the *infinitesimal rotation vectors*. They are connected to the variations δs and $\delta_{12} s$ of the quaternion by

$$\begin{aligned} \delta s &= \tfrac{1}{2}\, \delta \hat{\boldsymbol{s}}\, s \\ \delta_{12} s &= \left(\tfrac{1}{2}\, \delta_{12} \hat{\boldsymbol{s}} - \tfrac{1}{4}\, \delta_1 \hat{\boldsymbol{s}} \cdot \delta_2 \hat{\boldsymbol{s}} \right) s. \end{aligned} \tag{B.1}$$

The increment $\delta \hat{\boldsymbol{s}}$ is linear with respect to the variation $\delta \boldsymbol{X}$ of the degrees of freedom, and the increment $\delta_{12}\hat{\boldsymbol{s}}$ is bilinear with respect to the independent variations $\delta_1 \boldsymbol{X}$ and $\delta_2 \boldsymbol{X}$ of the degrees of freedom. As usual in our notation, $\delta_1 \hat{\boldsymbol{s}}$ and $\delta_2 \hat{\boldsymbol{s}}$ denote the first-order variation $\delta \hat{\boldsymbol{s}}$, evaluated on the increment $\delta_1 \boldsymbol{X}$ and $\delta_2 \boldsymbol{X}$, respectively. This representation of the first and second variations of a parameterized quaternion is equivalent to that proposed by [10].

The proof is as follows. By taking the first variation of the condition $2\,(s\,\overline{s} - 1) = 0$ that s is a unit quaternion, we have $0 = 2\,\delta s\,\overline{s} + 2\,s\,\overline{\delta s} = 2\,\delta s\,\overline{s} + \overline{2\,\delta s\,\overline{s}}$. This shows that the quaternion $2\,\delta s\,\overline{s}$ is a pure vector: this the vector $\delta \hat{\boldsymbol{s}}$ introduced in equation (B.1) above. Now, by inserting the increment $\delta_1 \boldsymbol{X}$ in the relation just derived, we have $2\,\delta_1 s\,\overline{s} \in \mathbb{R}^3$; perturbing this expression as $s \leftarrow s + \delta_2 s$, one shows that the following quaternion is a pure vector: $2\,\delta_{12} s\,\overline{s} + 2\,\delta_1 s\,\overline{\delta_2 s} = 2\,\delta_{12} s\,\overline{s} + \frac{1}{2}\,(\delta_1 \hat{\boldsymbol{s}}\, s)\,\overline{(\delta_2 \hat{\boldsymbol{s}}\, s)} = 2\,\delta_{12} s\,\overline{s} - \frac{1}{2}\,\delta_1 \hat{\boldsymbol{s}}\,\delta_2 \hat{\boldsymbol{s}} = 2\,\delta_{12} s\,\overline{s} + \frac{1}{2}\,\delta_1 \hat{\boldsymbol{s}} \cdot \delta_2 \hat{\boldsymbol{s}} - \frac{1}{2}\,\delta_1 \hat{\boldsymbol{s}} \times \delta_2 \hat{\boldsymbol{s}}$; here, the quaternion product $\delta_1 \hat{\boldsymbol{s}}\,\delta_2 \hat{\boldsymbol{s}}$ has been evaluated using the definition (2.1). Adding the vector quantity $\frac{1}{2}\,\delta_1 \hat{\boldsymbol{s}} \times \delta_2 \hat{\boldsymbol{s}}$, the quantity $2\,\delta_{12} s\,\overline{s} + \frac{1}{2}\,\delta_1 \hat{\boldsymbol{s}} \cdot \delta_2 \hat{\boldsymbol{s}}$ appears to be another pure vector: this is the vector $\delta_{12}\hat{\boldsymbol{s}}$ introduced in equation (B.1).

The second-order infinitesimal rotation vector $\delta_{12}\hat{\boldsymbol{s}}$ can be calculated directly from the first-order one $\delta \hat{\boldsymbol{s}}$ as

$$\delta_{12}\hat{\boldsymbol{s}} = \frac{\delta_1(\delta_2 \hat{\boldsymbol{s}}) + \delta_2(\delta_1 \hat{\boldsymbol{s}})}{2}. \tag{B.2}$$

Here, $\delta_1(\delta_2 \hat{\boldsymbol{s}})$ denotes the first-order variation of $\delta_2 \hat{\boldsymbol{s}}$ when s is perturbed into $s + \delta_1 s$; this quantity is *not* symmetric with respect to the perturbations $\delta_1 s$ and $\delta_2 s$. Similarly, $\delta_2(\delta_1 \hat{\boldsymbol{s}})$ denotes the first-order variation of $\delta_1 \hat{\boldsymbol{s}}$ when s is perturbed into $s + \delta_2 s$.

The proof of equation (B.2) is as follows. Take the second variation of $\delta_1 s = \frac{1}{2}\,\delta_1 \hat{\boldsymbol{s}}\, s$ from equation (B.1) as $\delta_{12} s = \frac{1}{2}\,\delta_2(\delta_1 \hat{\boldsymbol{s}})\, s + \frac{1}{4}\,\delta_1 \hat{\boldsymbol{s}}\,\delta_2 \hat{\boldsymbol{s}}\, s = \left(\frac{1}{2}\,\delta_2(\delta_1 \hat{\boldsymbol{s}}) - \frac{1}{4}\,\delta_1 \hat{\boldsymbol{s}} \cdot \delta_2 \hat{\boldsymbol{s}} + \frac{1}{4}\,\delta_1 \hat{\boldsymbol{s}} \times \delta_2 \hat{\boldsymbol{s}} \right) s$. The left-hand side is symmetric with respect to the perturbations $\delta_1 s$ and $\delta_2 s$, by definition of the second variation. Symmetrizing the right-hand side, we obtain $\delta_{12} s = \left(\frac{\delta_1(\delta_2 \hat{\boldsymbol{s}}) + \delta_2(\delta_1 \hat{\boldsymbol{s}})}{4} - \frac{\delta_1 \hat{\boldsymbol{s}} \cdot \delta_2 \hat{\boldsymbol{s}}}{4} \right) s$. The infinitesimal rotation vector $\delta_{12}\hat{\boldsymbol{s}}$ can then be identified from equation (B.1), which yields the result stated in equation (B.2).

In the following sections, the first and second variations of the rotations that enter into the Discrete elastic rod model, such as the parallel transport p^i and the director rotation d^i, will be systematically represented using the corresponding infinitesimal rotation vectors, such as $\delta \hat{\boldsymbol{p}}^i$, $\delta_{12}\hat{\boldsymbol{p}}^i$, $\delta \hat{\boldsymbol{d}}^i$ and $\delta_{12}\hat{\boldsymbol{d}}^i$.

B.2 Variation of parallel transport

We start by deriving the variations of the parallel transport $p_{\boldsymbol{a}}^{\boldsymbol{b}}$ from the unit vector $\boldsymbol{a}$ to the unit vector $\boldsymbol{b}$ defined in equation (2.3), assuming $\boldsymbol{b} \neq -\boldsymbol{a}$. As $\boldsymbol{a}$ represents the fixed unit tangent $\boldsymbol{T}^i$ in reference configuration, it remains unperturbed,

$$\delta \boldsymbol{a} = \boldsymbol{0} \qquad \delta_{12} \boldsymbol{a} = \boldsymbol{0}.$$

Since $\boldsymbol{b}$ remains a unit vector during the perturbation, we have $\frac{1}{2}\left(|\boldsymbol{b}|^2-1\right)=0$. Taking the first and second variation of this constraint, we have

$$\boldsymbol{b}\cdot\delta\boldsymbol{b}=0 \qquad \boldsymbol{b}\cdot\delta_{12}\boldsymbol{b}+\delta_1\boldsymbol{b}\cdot\delta_2\boldsymbol{b}=\boldsymbol{0}.$$

B.2.1 First variation of parallel transport

As a preliminary step, we consider the case of parallel transport from $\boldsymbol{b}$ to its perturbation $\boldsymbol{b}+\delta\boldsymbol{b}$. Using $\boldsymbol{b}\cdot\delta\boldsymbol{b}=0$, we find from equation (2.3),

$$p_{\boldsymbol{b}}^{\boldsymbol{b}+\delta\boldsymbol{b}}=1+\frac{\boldsymbol{b}\times\delta\boldsymbol{b}}{2}+\mathcal{O}(|\delta\boldsymbol{b}|^2).$$

We now return to the calculation of $p_{\boldsymbol{a}}^{\boldsymbol{b}+\delta\boldsymbol{b}}$. Following the work of [12], as well as equations [3.7] and [A.2] from [26], one can use a holonomy reasoning to shows that, to first order in $\delta\boldsymbol{b}$,

$$p_{\boldsymbol{a}}^{\boldsymbol{b}+\delta\boldsymbol{b}}=p_{\boldsymbol{b}}^{\boldsymbol{b}+\delta\boldsymbol{b}}\,p_{\boldsymbol{a}}^{\boldsymbol{b}}\,r_{\boldsymbol{a}}\left(-\frac{\boldsymbol{a}\times\boldsymbol{b}}{1+\boldsymbol{a}\cdot\boldsymbol{b}}\cdot\delta\boldsymbol{b}\right)+\mathcal{O}(|\delta\boldsymbol{b}|^2).$$

We rewrite this as

$$p_{\boldsymbol{a}}^{\boldsymbol{b}+\delta\boldsymbol{b}}=p_{\boldsymbol{b}}^{\boldsymbol{b}+\delta\boldsymbol{b}}\,p_{\boldsymbol{a}}^{\boldsymbol{b}}\,r_{\boldsymbol{a}}(\delta\theta)+\mathcal{O}(|\delta\boldsymbol{b}|^2), \tag{B.3}$$

where $\delta\theta=-\frac{\boldsymbol{k}}{2}\cdot\delta\boldsymbol{b}$ and $\boldsymbol{k}$ is the scaled binormal that characterizes the holonomy (see [12]),

$$\boldsymbol{k}=\frac{2\,\boldsymbol{a}\times\boldsymbol{b}}{1+\boldsymbol{a}\cdot\boldsymbol{b}}. \tag{B.4}$$

The infinitesimal rotation $r_{\boldsymbol{a}}(\delta\theta)$ from equation (B.3) can be found from equation (2.2) as

$$\begin{aligned} r_{\boldsymbol{a}}(\delta\theta) &= 1+\boldsymbol{a}\,\tfrac{\delta\theta}{2}+\mathcal{O}(\delta\theta^2)\\ &= 1-\tfrac{\boldsymbol{k}\cdot\delta\boldsymbol{b}}{4}\,\boldsymbol{a}+\mathcal{O}(\delta\theta^2)\\ &= 1-\tfrac{\boldsymbol{a}\otimes\boldsymbol{k}}{4}\cdot\delta\boldsymbol{b}+\mathcal{O}(\delta\theta^2). \end{aligned} \tag{B.5}$$

Equation (B.3) is then rewritten with the help of the operator $\boldsymbol{b}_\times$ from equation (3.3) as

$$\begin{aligned} p_{\boldsymbol{a}}^{\boldsymbol{b}+\delta\boldsymbol{b}} &= \left(1+\tfrac{\boldsymbol{b}_\times}{2}\cdot\delta\boldsymbol{b}\right)p_{\boldsymbol{a}}^{\boldsymbol{b}}\left(1-\tfrac{\boldsymbol{a}\otimes\boldsymbol{k}}{4}\cdot\delta\boldsymbol{b}\right)+\mathcal{O}(|\delta\boldsymbol{b}|^2)\\ &= \left(1+\tfrac{\boldsymbol{b}_\times}{2}\cdot\delta\boldsymbol{b}-\tfrac{(p_{\boldsymbol{a}}^{\boldsymbol{b}}*\boldsymbol{a})\otimes\boldsymbol{k}}{4}\cdot\delta\boldsymbol{b}\right)p_{\boldsymbol{a}}^{\boldsymbol{b}}+\mathcal{O}(|\delta\boldsymbol{b}|^2)\\ &= \left(1+\tfrac{2\,\boldsymbol{b}_\times-\boldsymbol{b}\otimes\boldsymbol{k}}{4}\cdot\delta\boldsymbol{b}\right)p_{\boldsymbol{a}}^{\boldsymbol{b}}+\mathcal{O}(|\delta\boldsymbol{b}|^2). \end{aligned}$$

In view of this, the first order variation of parallel transport writes as

$$\delta p_{\boldsymbol{a}}^{\boldsymbol{b}}=\frac{1}{2}\left(\left(\boldsymbol{b}_\times-\frac{\boldsymbol{b}\otimes\boldsymbol{k}}{2}\right)\cdot\delta\boldsymbol{b}\right)p_{\boldsymbol{a}}^{\boldsymbol{b}}.$$

Identifying with equation (B.1), we find that it is captured by the infinitesimal rotation vector

$$\delta\hat{\boldsymbol{p}}_{\boldsymbol{a}}^{\boldsymbol{b}}=\left(\boldsymbol{b}_\times-\frac{\boldsymbol{b}\otimes\boldsymbol{k}}{2}\right)\cdot\delta\boldsymbol{b}. \tag{B.6}$$

B.2.2 Second variation of parallel transport

From equation (B.6), we have

$$\begin{aligned} \delta_2(\delta_1\hat{\boldsymbol{p}}_{\boldsymbol{a}}^{\boldsymbol{b}}) &= \left((\delta_2\boldsymbol{b})_\times-\tfrac{\delta_2\boldsymbol{b}\otimes\boldsymbol{k}+\boldsymbol{b}\otimes\delta_2\boldsymbol{k}}{2}\right)\cdot\delta_1\boldsymbol{b}+\left(\boldsymbol{b}_\times-\tfrac{\boldsymbol{b}\otimes\boldsymbol{k}}{2}\right)\cdot\delta_{12}\boldsymbol{b}\\ &= \delta_2\boldsymbol{b}\times\delta_1\boldsymbol{b}-\tfrac{1}{2}\delta_2\boldsymbol{b}\,(\boldsymbol{k}\cdot\delta_1\boldsymbol{b})-\tfrac{\boldsymbol{b}}{2}\,\delta_2\boldsymbol{k}\cdot\delta_1\boldsymbol{b}+\left(\boldsymbol{b}_\times-\tfrac{\boldsymbol{b}\otimes\boldsymbol{k}}{2}\right)\cdot\delta_{12}\boldsymbol{b} \end{aligned} \tag{B.7}$$

Using equation (B.4), the variation of the binormal is found as

$$\begin{aligned}\delta_2\boldsymbol{k} &= \tfrac{2\,\boldsymbol{a}\times\delta_2\boldsymbol{b}}{1+\boldsymbol{a}\cdot\boldsymbol{b}} - \tfrac{2\,\boldsymbol{a}\times\boldsymbol{b}}{(1+\boldsymbol{a}\cdot\boldsymbol{b})^2}\,\boldsymbol{a}\cdot\delta_2\boldsymbol{b} \\ &= \tfrac{2}{1+\boldsymbol{a}\cdot\boldsymbol{b}}\left(\boldsymbol{a}\times\delta_2\boldsymbol{b} - \tfrac{\boldsymbol{k}}{2}(\boldsymbol{a}\cdot\delta_2\boldsymbol{b})\right) \\ &= \tfrac{2}{1+\boldsymbol{a}\cdot\boldsymbol{b}}\left(\boldsymbol{a}_\times - \tfrac{\boldsymbol{k}\otimes\boldsymbol{a}}{2}\right)\cdot\delta_2\boldsymbol{b}\end{aligned}$$

Inserting into equation (B.7) and reordering the terms, we find

$$\delta_2(\delta_1\hat{\boldsymbol{p}}_{\boldsymbol{a}}^{\boldsymbol{b}}) = \delta_2\boldsymbol{b}\times\delta_1\boldsymbol{b} + \left(\boldsymbol{b}_\times - \frac{\boldsymbol{b}\otimes\boldsymbol{k}}{2}\right)\cdot\delta_{12}\boldsymbol{b} - \frac{\boldsymbol{b}}{(1+\boldsymbol{a}\cdot\boldsymbol{b})}\left(\delta_1\boldsymbol{b}\cdot\left(\boldsymbol{a}_\times - \frac{\boldsymbol{k}\otimes\boldsymbol{a}}{2}\right)\cdot\delta_2\boldsymbol{b}\right) - \frac{\delta_2\boldsymbol{b}\otimes\delta_1\boldsymbol{b}}{2}\cdot\boldsymbol{k}$$

In view of equation (B.2), we can obtain the second-order infinitesimal rotation vector by symmetrizing this with respect to the increments $\delta_1\boldsymbol{b}$ and $\delta_2\boldsymbol{b}$:

$$\begin{aligned}\delta_{12}\hat{\boldsymbol{p}}_{\boldsymbol{a}}^{\boldsymbol{b}} &= \tfrac{\delta_2(\delta_1\hat{\boldsymbol{p}}_{\boldsymbol{a}}^{\boldsymbol{b}})+\delta_1(\delta_2\hat{\boldsymbol{p}}_{\boldsymbol{a}}^{\boldsymbol{b}})}{2} \\ &= \left(\boldsymbol{b}_\times - \tfrac{\boldsymbol{b}\otimes\boldsymbol{k}}{2}\right)\cdot\delta_{12}\boldsymbol{b} + \left(\delta_1\boldsymbol{b}\cdot\tfrac{\boldsymbol{k}\otimes\boldsymbol{a}+\boldsymbol{a}\otimes\boldsymbol{k}}{4\,(1+\boldsymbol{a}\cdot\boldsymbol{b})}\cdot\delta_2\boldsymbol{b}\right)\boldsymbol{b} - \tfrac{(\delta_1\boldsymbol{b}\otimes\delta_2\boldsymbol{b}+\delta_2\boldsymbol{b}\otimes\delta_1\boldsymbol{b})}{2}\cdot\tfrac{\boldsymbol{k}}{2}.\end{aligned} \tag{B.8}$$

B.2.3 Application to a Discrete elastic rod

In a Discrete elastic rod, the transport is from the undeformed tangent $\boldsymbol{a} = \boldsymbol{T}^i$ to the deformed tangent $\boldsymbol{b} = \boldsymbol{t}^i$, see equation (2.9). Equation (B.4) then yields the definition of the binormal $\boldsymbol{k}^i$ announced in equation (3.4), and equation (B.6) yields the expression for $\delta\hat{\boldsymbol{p}}^i$ announced in equation (3.2). In equation (B.8), condensing the independent variations as $\delta_1\boldsymbol{b} = \delta_2\boldsymbol{b} = \delta\boldsymbol{t}^i$ and identifying $\delta_{12}\hat{\boldsymbol{p}}_{\boldsymbol{a}}^{\boldsymbol{b}} = \delta^2\hat{\boldsymbol{p}}^i$ and $\delta_{12}\boldsymbol{b} = \delta^2\boldsymbol{t}^i$ yields the expression of $\delta^2\hat{\boldsymbol{p}}^i$ announced in equation (3.2).

B.3 Variation of unit tangents

With $\boldsymbol{E}^i = \boldsymbol{x}_{i+1} - \boldsymbol{x}_i$ as the segment vector, the variation of the unit tangent $\boldsymbol{t}^i = \boldsymbol{E}^i/|\boldsymbol{E}^i|$ from equation (2.6) writes

$$\begin{aligned}\delta\boldsymbol{t}^i &= \tfrac{\delta\boldsymbol{E}^i}{|\boldsymbol{E}^i|} - \boldsymbol{E}^i\tfrac{\delta(|\boldsymbol{E}^i|)}{|\boldsymbol{E}^i|^2} \\ &= \tfrac{\delta\boldsymbol{E}^i}{|\boldsymbol{E}^i|} - \boldsymbol{E}^i\tfrac{(\boldsymbol{E}^i\cdot\delta\boldsymbol{E}^i)}{|\boldsymbol{E}^i|^3} \\ &= \tfrac{\boldsymbol{I}-\boldsymbol{t}^i\otimes\boldsymbol{t}^i}{|\boldsymbol{E}^i|}\cdot\delta_1\boldsymbol{E}^i\end{aligned}$$

With $\delta\boldsymbol{E}^i = \delta\boldsymbol{x}_{i+1} - \delta\boldsymbol{x}_i$, this is the expression of the first variation announced in equation (3.1).

Next, the second variation is calculated as

$$\delta_{12}\boldsymbol{t}^i = \left(-\frac{\delta_2\boldsymbol{t}^i\otimes\boldsymbol{t}^i + \boldsymbol{t}^i\otimes\delta_2\boldsymbol{t}^i}{|\boldsymbol{E}^i|} - \frac{(\boldsymbol{I}-\boldsymbol{t}^i\otimes\boldsymbol{t}^i)}{|\boldsymbol{E}^i|^2}\,\frac{\boldsymbol{E}^i\cdot\delta_2\boldsymbol{E}^i}{|\boldsymbol{E}^i|}\right)\cdot\delta_1\boldsymbol{E}^i.$$

Here, we have used $\delta_{12}\boldsymbol{E}^i = \boldsymbol{0}$ since $\boldsymbol{E}^i = \boldsymbol{x}_{i+1} - \boldsymbol{x}_i$ depends linearly on the degrees of freedom. Inserting the expression of the first variations from equation (3.1), the second variation $\delta_{12}\boldsymbol{t}^i$ can be rewritten as

$$\begin{aligned}\delta_{12}\boldsymbol{t}^i &= \left(-\tfrac{((\boldsymbol{I}-\boldsymbol{t}^i\otimes\boldsymbol{t}^i)\cdot\delta_2\boldsymbol{E}^i)\otimes\boldsymbol{t}^i+\boldsymbol{t}^i\otimes((\boldsymbol{I}-\boldsymbol{t}^i\otimes\boldsymbol{t}^i)\cdot\delta_2\boldsymbol{E}^i)}{|\boldsymbol{E}^i|^2} - \tfrac{(\boldsymbol{I}-\boldsymbol{t}^i\otimes\boldsymbol{t}^i)}{|\boldsymbol{E}^i|^2}\boldsymbol{t}^i\cdot\delta_2\boldsymbol{E}^i\right)\cdot\delta_1\boldsymbol{E}^i \\ &= -\tfrac{\tau^i_{IKJ}+\tau^i_{JKI}+\tau^i_{IJK}}{|\boldsymbol{E}^i|^2}\,(\delta_1E^i)_J\,(\delta_2E^i)_K\,\boldsymbol{e}_I \\ &= -\tfrac{((\boldsymbol{\tau}^i)^{T(132)}+(\boldsymbol{\tau}^i)^{T(231)}+\boldsymbol{\tau}^i)_{IJK}}{|\boldsymbol{E}^i|^2}\,(\delta_1E^i)_J\,(\delta_2E^i)_K\,\boldsymbol{e}_I \\ &= -\tfrac{\boldsymbol{\tau}^i+(\boldsymbol{\tau}^i)^{T(132)}+(\boldsymbol{\tau}^i)^{T(231)}}{|\boldsymbol{E}^i|^2} : ((\delta_1\boldsymbol{x}_{i+1}-\delta_1\boldsymbol{x}_i)\otimes(\delta_2\boldsymbol{x}_{i+1}-\delta_2\boldsymbol{x}_i)),\end{aligned}$$

where the third-order tensor $\boldsymbol{\tau}^i = (\boldsymbol{I}-\boldsymbol{t}^i\otimes\boldsymbol{t}^i)\otimes\boldsymbol{t}^i$ and its generalized transpose are defined below equation (3.1). The expression of $\delta^2\boldsymbol{t}^i$ announced in equation (3.1) is obtained by condensing $\delta_1\boldsymbol{x}_i = \delta_2\boldsymbol{x}_i = \delta\boldsymbol{x}_i$ and identifying $\delta^2\boldsymbol{t}^i = \delta_{12}\boldsymbol{t}^i$.

B.4 Variation of directors rotation

In view of equation (B.1), the infinitesimal rotation vector $\delta\hat{\boldsymbol{d}}^i$ associated with the directors rotation d^i is

$$\delta\hat{\boldsymbol{d}}^i = 2\,\delta d^i\,\overline{d}^i.$$

Differentiating the expression of d^i from equation (2.8), we have $\delta d^i = \delta\left(p^i\,r_{\boldsymbol{T}^i}(\varphi^i)\,D^i\right) = \delta p^i\,r_{\boldsymbol{T}^i}(\varphi^i)\,D^i + p^i\,\delta(r_{\boldsymbol{T}^i}(\varphi^i))\,D^i$. Equation (2.2) shows that, with a fixed unit vector $\boldsymbol{T}^i$, $\delta(r_{\boldsymbol{T}^i}(\varphi^i)) = \frac{1}{2}\left[\delta\varphi^i\,\boldsymbol{T}^i\right]\,r_{\boldsymbol{T}^i}(\varphi^i)$—here, the vector in square bracket is an infinitesimal rotation vector, see equation (B.1). This yields $\delta d^i = \delta p^i\,r_{\boldsymbol{T}^i}(\varphi^i)\,D^i + \frac{1}{2}\,p^i\,\delta\varphi^i\,\boldsymbol{T}^i\,r_{\boldsymbol{T}^i}(\varphi^i)\,D^i$. Inserting into the equation above, and using $\overline{d}^i = \overline{D}^i\,r_{\boldsymbol{T}^i}(-\varphi^i)\,\overline{p}^i$ from equation (2.8), we find

$$\begin{aligned}
\delta\hat{\boldsymbol{d}}^i &= \delta\varphi^i\,p^i\,\boldsymbol{T}^i\,r_{\boldsymbol{T}^i}(\varphi^i)\,D^i\,\overline{d}^i + 2\,\delta p^i\,r_{\boldsymbol{T}^i}(\varphi^i)\,D^i\,\overline{d}^i \\
&= \delta\varphi^i\,p^i\,\boldsymbol{T}^i\,\overline{p}^i + 2\,\delta p^i\,\overline{p}^i \\
&= \delta\varphi^i\,p^i * \boldsymbol{T}^i + \delta\hat{\boldsymbol{p}}^i \\
&= \delta\varphi^i\,\boldsymbol{t}^i + \delta\hat{\boldsymbol{p}}^i,
\end{aligned}$$

as announced in equation (3.5).

The second-order infinitesimal rotation vector is then obtained from equation (B.2) as

$$\begin{aligned}
\delta_{12}\hat{\boldsymbol{d}}^i &= \tfrac{1}{2}\left(\delta_2\left(\delta_1\varphi^i\,\boldsymbol{t}^i + \delta_1\hat{\boldsymbol{p}}^i\right) + \delta_1\left(\delta_2\varphi^i\,\boldsymbol{t}^i + \delta_2\hat{\boldsymbol{p}}^i\right)\right) \\
&= \tfrac{\delta_1\varphi^i\,\delta_2\boldsymbol{t}^i + \delta_2\varphi^i\,\delta_1\boldsymbol{t}^i}{2} + \delta_{12}\hat{\boldsymbol{p}}^i.
\end{aligned}$$

Here, we have used $\delta_{12}\varphi^i = 0$ as φ^i is a degree of freedom and the variations $\delta_1\varphi^i$ and $\delta_2\varphi^i$ are independent.

Upon condensation of the two variations, the equation leads to the expression of $\delta^2\hat{\boldsymbol{d}}^i$ announced in equation (3.5).

B.5 Rotation gradient

In view of equation (B.1), the infinitesimal rotation vector $\delta\hat{\boldsymbol{q}}_i$ associated with the rotation gradient $q_i = \overline{d^{i-1}}d^i$ from equation (2.11) writes

$$\begin{aligned}
\delta\hat{\boldsymbol{q}}_i &= 2\,\delta q_i\,\overline{q_i} \\
&\quad \left(\overline{2\,\delta d^{i-1}}\,d^i + \overline{d^{i-1}}\,2\,\delta d^i\right)\,\overline{q_i} \\
&= \overline{d^{i-1}}\,(-\delta\hat{\boldsymbol{d}}^{i-1} + \delta\hat{\boldsymbol{d}}^i)\,d^{i-1}
\end{aligned}$$

as announced in equation (3.6).

The following identity yields the variation of the vector $\overline{s} * \boldsymbol{u}$ obtained by applying the inverse $\overline{s}$ of a rotation s to a vector $\boldsymbol{u}$,

$$\begin{aligned}
\delta(\overline{s} * \boldsymbol{u}) &= \delta\left(\overline{s}\,\boldsymbol{u}\,s\right) \\
&= \overline{\delta s}\,\boldsymbol{u}\,s + \overline{s}\,\boldsymbol{u}\,\delta s + \overline{s}\,\delta\boldsymbol{u}\,s \\
&= \tfrac{-\overline{s}\,\delta\hat{\boldsymbol{s}}\,\boldsymbol{u}\,\overline{s} + \overline{s}\,\boldsymbol{u}\,\delta\hat{\boldsymbol{s}}\,s}{2} + \overline{s} * \delta\boldsymbol{u} \\
&= \tfrac{-(\overline{s} * \delta\hat{\boldsymbol{s}})\,(\overline{s} * \boldsymbol{u}) + (\overline{s} * \boldsymbol{u})\,(\overline{s} * \delta\hat{\boldsymbol{s}})}{2} + \overline{s} * \delta\boldsymbol{u} \\
&= -(\overline{s} * \delta\hat{\boldsymbol{s}}) \times (\overline{s} * \boldsymbol{u}) + \overline{s} * \delta\boldsymbol{u}.
\end{aligned}$$

With $\delta = \delta_1$, $s = d^{i-1}$ and $\boldsymbol{u} = \delta_2\hat{\boldsymbol{d}}^i - \delta_2\hat{\boldsymbol{d}}^{i-1}$, we have $\overline{s} * \boldsymbol{u} = \overline{d^{i-1}} * (\delta_2\hat{\boldsymbol{d}}^i - \delta_2\hat{\boldsymbol{d}}^{i-1}) = \delta_2\hat{\boldsymbol{q}}_i$, see equation (3.6), and the identity above yields

$$\begin{aligned}
\delta_1(\delta_2\hat{\boldsymbol{q}}_i) &= -(\overline{d^{i-1}} * \delta_1\hat{\boldsymbol{d}}^{i-1}) \times \delta_2\hat{\boldsymbol{q}}_i + \overline{d^{i-1}} * (\delta_1(\delta_2\hat{\boldsymbol{d}}^i) - \delta_1(\delta_2\hat{\boldsymbol{d}}^{i-1})) \\
&= \overline{d^{i-1}} * (\delta_1(\delta_2\hat{\boldsymbol{d}}^i) - \delta_1(\delta_2\hat{\boldsymbol{d}}^{i-1})) + \delta_2\hat{\boldsymbol{q}}_i \times (\overline{d^{i-1}} * \delta_1\hat{\boldsymbol{d}}^{i-1})
\end{aligned}.$$

Symmetrizing with respect to the independent variations δ_1 and δ_2 and using equation (B.2), we obtain the second infinitesimal vector as

$$\delta_{12}\hat{\boldsymbol{q}}_i = \overline{d^{i-1}} * \left(\delta_{12}\hat{\boldsymbol{d}}^i - \delta_{12}\hat{\boldsymbol{d}}^{i-1}\right) + \frac{\delta_1\hat{\boldsymbol{q}}_i \times (\overline{d^{i-1}} * \delta_2\hat{\boldsymbol{d}}^{i-1}) + \delta_2\hat{\boldsymbol{q}}_i \times (\overline{d^{i-1}} * \delta_1\hat{\boldsymbol{d}}^{i-1})}{2}.$$

Upon condensation of the two variations, the equation leads to the expression of $\delta^2\hat{\boldsymbol{q}}_i$ announced in equation (3.6).

B.6 Strain vector

Equation (2.13) can be rewritten as $\boldsymbol{\kappa}_i = 2\,\mathcal{I}(q_i)$, where $\mathcal{I}(q) = \frac{q-\overline{q}}{2}$ denotes the vector part of a quaternion. The operator $\mathcal{I}$ being linear, we have

$$\begin{aligned} \delta\boldsymbol{\kappa}_i &= 2\,\mathcal{I}(\delta q_i) \\ &= \mathcal{I}\left(\delta\hat{\boldsymbol{q}}_i\, q_i\right) \end{aligned}$$

as well as

$$\begin{aligned} \delta_{12}\boldsymbol{\kappa}_i &= 2\,\mathcal{I}(\delta_{12} q_i) \\ &= \mathcal{I}\left(\left(\delta_{12}\hat{\boldsymbol{q}}_i - \tfrac{\delta_1\hat{\boldsymbol{q}}_i\cdot\delta_2\hat{\boldsymbol{q}}_i}{2}\right) q_i\right), \end{aligned}$$

as announced in equation (3.7). In the equation above, the second variation of the unit quaternion $\delta_{12}q_i$ has been expressed using equation (B.1).

References

[1] S.S. Antman. *Nonlinear problems of elasticity.* Springer-Verlag, 2005.

[2] B. Audoly, N. Clauvelin, P.-T. Brun, M. Bergou, E. Grinspun, and M. Wardetzky. A discrete geometric approach for simulating the dynamics of thin viscous threads. *Journal of Computational Physics*, 253:18–49, 2013.

[3] B. Audoly and J. W. Hutchinson. Analysis of necking based on a one-dimensional model. *Journal of the Mechanics and Physics of Solids*, 97:68–91, 2016.

[4] B. Audoly and J. W. Hutchinson. One-dimensional modeling of necking in rate-dependent materials. *Journal of the Mechanics and Physics of Solids*, 123:149–171, 2019.

[5] B. Audoly and S. Neukirch. A one-dimensional model for elastic ribbons: a little stretching makes a big difference. *Journal of the Mechanics and Physics of Solids*, 153:104457, 2021.

[6] B. Audoly and Y. Pomeau. *Elasticity and geometry: from hair curls to the nonlinear response of shells.* Oxford University Press, 2010.

[7] B. Audoly and K. A. Seffen. Buckling of naturally curved elastic strips: the ribbon model makes a difference. *Journal of Elasticity*, 119(1):293–320, 2015.

[8] J. Bae, J.-H. Na, C. D. Santangelo, and R. C. Hayward. Edge-defined metric buckling of temperature-responsive hydrogel ribbons and rings. *Polymer*, 55(23):5908–5914, 2014.

[9] C. Baek and P. M. Reis. Rigidity of hemispherical elastic gridshells under point load indentation. *Journal of the Mechanics and Physics of Solids*, 124:411–426, 2019.

[10] J. Barbič and Y. Zhao. Real-time large-deformation substructuring. In *ACM SIGGRAPH 2011 Papers*, pages 1–8, New York, NY, USA, 2011. Association for Computing Machinery.

[11] M. Bergou, B. Audoly, E. Vouga, M. Wardetzky, and E. Grinspun. Discrete viscous threads. *Transactions on Graphics*, 29(4):116, 2010.

[12] M. Bergou, M. Wardetzky, S. Robinson, B. Audoly, and E. Grinspun. Discrete elastic rods. *ACM Transactions on Graphics*, 27(3):63:1–63:12, 2008.

[13] F. Bertails, B. Audoly, M-P. Cani, B. Querleux, F. Leroy, and J.-L. Lévêque. Super-helices for predicting the dynamics of natural hair. In *ACM Transactions on Graphics*, pages 1180–1187, August 2006.

[14] P.-T. Brun, N. M. Ribe, and B. Audoly. A numerical investigation of the fluid mechanical sewing machine. *Physics of fluids*, 24(4):043102, 2012.

[15] R. Casati and F. Bertails-Descoubes. Super space clothoids. *ACM Transactions on Graphics*, 32(4), 2013.

[16] R. Charrondière, F. Bertails-Descoubes, S. Neukirch, and R. Romero. Numerical modeling of inextensible elastic ribbons with curvature-based elements. *Computer Methods in Applied Mechanics and Engineering*, 364:112922, 2020.

[17] B. D. Coleman and D. C. Newman. On the rheology of cold drawing. I. elastic materials. *Journal of Polymer Science: Part B: Polymer Physics*, 26:1801–1822, 1988.

[18] M. A. Dias and B. Audoly. "Wunderlich, meet Kirchhoff": A general and unified description of elastic ribbons and thin rods. *Journal of Elasticity*, 119(1):49–66, 2015.

[19] E. J. Doedel, A. R. Champneys, T. F. Fairgrieve, Y. A. Kuznetsov, B. Sandstede, and X. J. Wang. AUTO-07p: continuation and bifurcation software for ordinary differential equations. See http://indy.cs.concordia.ca/auto/, 2007.

[20] L. Freddi, P. Hornung, M.-G. Mora, and R. Paroni. A corrected Sadowsky functional for inextensible elastic ribbons. *Journal of Elasticity*, 123:125–136, 2015.

[21] M. Gazzola, L. H. Dudte, A. G. McCormick, and L. Mahadevan. Forward and inverse problems in the mechanics of soft filaments. *Royal Society Open Science*, 5(6), 2018.

[22] A. H. Gelebart, D. J. Mulder, M. Varga, A. Konya, G. Vantome, E. W. Meijer, R. L. B. Selinger, and D. J. Broer. Making waves in a photoactive polymer film. *Nature*, 546:632–636, 2017.

[23] Gaël Guennebaud, Benoît Jacob, et al. Eigen v3. http://eigen.tuxfamily.org, 2010.

[24] M. K. Jawed, A. Novelia, and O. M. O'Reilly. *A primer on the kinematics of discrete elastic rods*. Springer, 2017.

[25] C. Lestringant and B. Audoly. A one-dimensional model for elasto-capillary necking. *Proceedings of the Royal Society A*, 476(2240), 2020.

[26] C. Lestringant, B. Audoly, and D. M. Kochmann. A discrete, geometrically exact method for simulating nonlinear, elastic or non-elastic beams. *Computer Methods in Applied Mechanics and Engineering*, 361:112741, 2020.

[27] J. Linn. Discrete Cosserat rod kinematics constructed on the basis of the difference geometry of framed curves—part I: Discrete Cosserat curves on a staggered grid. *Journal of Elasticity*, pages 177–236, 2020.

[28] P.-O. Mouthuy, M. Coulombier, T. Pardoen, J.-P. Raskin, and A. M. Jonas. Overcurvature describes the buckling and folding of rings from curved origami to foldable tents. *Nature Communications*, 3(1):1–8, 2012.

[29] J. Nocedal and S. J. Wright. *Numerical Optimization*. Springer New York, 2006.

[30] J. Panetta, M. Konaković-Luković, F. Isvoranu, E. Bouleau, and M. Pauly. X-shells: A new class of deployable beam structures. *ACM Transactions on Graphics (Proceedings of SIGGRAPH)*, 2019.

[31] R. Paroni and G. Tomassetti. Macroscopic and microscopic behavior of narrow elastic ribbons. *Journal of Elasticity*, pages 409–433, 2019.

[32] N. M. Ribe, M. Habibi, and D. Bonn. Liquid rope coiling. *Annual Review of Fluid Mechanics*, 44:249–266, 2012.

[33] M. Sadowsky. Die Differentialgleichungen des Möbiusschen Bandes. In *Jahresbericht der Deutschen Mathematiker-Vereinigung*, volume 39 (2. Abt. Heft 5/8), pages 49–51, 1929.

[34] Tomohiko G. Sano and Hirofumi Wada. Twist-induced snapping in a bent elastic rod and ribbon. *Physical Review Letters*, 122(11):114301, 2019.

[35] E. L. Starostin and G. H. M. van der Heijden. The shape of a Möbius strip. *Nature Materials*, 6(8):563–567, 2007.

[36] E. L. Starostin and G. H. M. van der Heijden. Force and moment balance equations for geometric variational problems on curves. *Physical Review E*, 79:066602, Jun 2009.

[37] E. L. Starostin and G. H. M. van der Heijden. Equilibrium shapes with stress localisation for inextensible elastic möbius and other strips. *Journal of Elasticity*, 119(1):67–112, 2015.

[38] D. J. Steigmann and M. G. Faulkner. Variational theory for spatial rods. *Journal of Elasticity*, 33(1):1–26, 1993.

[39] A. C. Ugural and S. K. Fenster. *Advanced mechanics of materials and applied elasticity*. International Series in the Physical and Chemical Engineering Sciences. Prentice Hall, 2019.

[40] W. Wunderlich. Über ein abwickelbares Möbiusband. *Monatshefte für Mathematik*, 66(3):276–289, 1962.

[41] Yanlei Yu, Makoto Nakano, and Tomiki Ikeda. Photomechanics: Directed bending of a polymer film by light. *Nature*, 425(6954):145–145, 09 2003.